Sentinel-5 Precursor + Innovation: Sentinel-5 Precursor Ocean Color (S5POC) Product

Diffuse attenuation (K_d) product in Sentinel-5-p (S5p) Productive Algorithm Laboratory (PAL): Algorithm Theoretical Base Document (ATBD)

A. Bracher[1,2] J. Oelker[1,2] A. J. Bellido Rosas[1,2] A. Richter[2]

Date: Dec 20, 2024

[1]Alfred Wegener Institute (AWI), Helmholtz Centre for Polar and Marine Research, Busses-traße 24, D-27570 Bremerhaven, Germany

[2]Institute of Environmental Physics (IUP), University of Bremen, Otto-Hahn-Allee 1, D-28359 Bremen, Germany

Change log

Version Nr.	Date	Status	Change
1.0	Dec 20, 2024	ATBDv1	Final version for PAL

Contents

List of Figures

List of Tables

List of Abbreviations

AOD Aerosol Optical Depth

AWI Alfred Wegener Institute Helmholtz Centre for Polar and Marine Research

CDOM Colored dissolved organic matter

CCD Charge-coupled device

Chla Chlorophyll-a concentration

DOAS Differential Optical Absorption Spectroscopy

fMSE fractional mean squared error

GOME-2 Global Ozone Monitoring Experiment-2

HITRAN High-resolution transmission molecular absorption database

IOP Inherent Optical Properties

IUP Institute of Environmental Physics

K_d Diffuse attenuation coefficient

LUT Look-up Table

MAE Mean absolute error

MODIS-Aqua Moderate Resolution Imaging Spectroradiometer-Aqua

NIR Near-infrared

OC-PFT Algorithm of Hirata et al. (2011) to retrieve phytoplankton functional types

OLCI Ocean and Land Colour Instrument

OMI Ozone Monitoring Instrument

PACE Plankton, Aerosol, Cloud and ocean Ecosystem

PFT Phytoplankton Functional Type

PhytoDOAS DOAS applied for retrieval of phytoplankton biomass

RB	Requirements Baseline
RMSD	Root mean squared difference
RRS	Rotational Raman Scattering
RTM	Radiative Transfer Model
S5p	Sentinel-5 Precursor
S5POC	Sentinel-5 Precursor Ocean Color
SCIAMACHY	Scanning Imaging Absorption Spectrometers for Atmospheric Chartography
SIF-marine	sun induced marine Chla fluorescence
SWIR	Shortwave infrared
SynSenPFT	Synergistic Exploitation of hyper- and multispectral Sentinel measurements to determine Phytoplankton Functional Types
SZA	Solar zenith angle
TC	Triple collocation
TChla	Total chlorophyll-a concentration
TOA	Top of Atmosphere
TROPOMI	Tropospheric Monitoring Instrument
UV	Ultraviolet
UVA	DOAS fit window in ultraviolet-A from 356.5 to 390 nm
UVAB	DOAS fit window in ultraviolet-A from 312.5 to 338.5 nm
VIS	Visible
VRS	Vibrational Raman Scattering
VZA	Viewing Zenith Angle

1 Document Overview

This document describes the theoretical basis and implementation of the Sentinel-5P Ocean Color (S5POC) level-2 TROPOMI products. Section 2 describes the TROPOMI instrument. Sentinel-5P Ocean Color (S5POC) level-2 TROPOMI products include the diffuse attenuation coefficients (K_d) at the UV-AB, UV-A and short blue wavelength range based on (Oelker *et al.*, 2022). These products are introduced in section 3. A detailed description of the S5POC K_d level 2 product algorithm follows in section 4. Feasibility of an operational processing of the S5POC products (S5p K_d) is discussed in section 5. Section 7 presents the methods used to calculate uncertainties for the products. Validation with *in situ* data is summed up in section 8.

2 TROPOMI instrument

The satellite Sentinel-5 Precursor (S5p) hosts the Tropospheric Monitoring Instrument (TROPOMI) (Veefkind *et al.*, 2012). It is in a low Earth orbit and its standard level 2 products provide daily global measurements of atmospheric trace gases and aerosols. The satellite was launched in October 2017. Local solar time at ascending node is 13:30. TROPOMI measures backscattered radiances at a spatial resolution of 3.5 km by 5.5 km (until 5 August 2019 at 3.5 km by 7 km) at nadir. Once per day the solar irradiance is recorded. Measurements are taken by a charge-coupled device (CCD) sensor at a swath width of 2600 km providing daily global coverage. TROPOMI has spectral bands in the ultraviolet (UV), the visible (VIS), near-infrared (NIR), and the shortwave infrared (SWIR). Relevant for developing ocean color products are band 3 (UV) from 310 nm to 405 nm, and band 4 (VIS) from 405 nm to 500 nm. The spectral resolution is 0.55 nm for bands 3 and 4.

3 Introduction to TROPOMI diffuse attenuation coefficient products

Traditionally, ocean color products are derived from multispectral sensors that record the backscattered radiance at 8 to 21 bands with a width of 10 to 20 nm in the VIS and NIR. Current multispectral sensors with daily global coverage have a spatial resolution below 500 m. Most ocean color retrievals are based on the water-leaving radiance which is acquired from the backscattered radiance by applying an atmospheric correction. The broad spectral resolution and limited number of bands of multispectral sensors limits the discrimination of the optical imprints of different water constituents. Hyperspectral ocean color sensors that continuously record the backscattered radiance at a spectral resolution of 5 nm or lower offer a new level for observing the ocean from space. Upcoming hyperspectral ocean color sensors such as the Plankton, Aerosol, Cloud and ocean Ecosystem (PACE) mission (https://pace.oceansciences.org/mission.htm) target a better spectral resolution of 5 nm which will allow for a better understanding of the phytoplankton ecology.

Atmospheric sensors measure the backscattered radiance at much higher spectral resolution, around 0.5 nm in the UV to NIR bands. It has been shown that measurements from these kind of sensors can be exploited to successfully retrieve phytoplankton functional types (Bracher *et al.*, 2009; Sadeghi *et al.*, 2012), light availability (Dinter *et al.*, 2015), diffuse attenuation (Dinter *et al.*, 2015; Oelker *et al.*, 2019, 2022), and sun-induced marine fluorescence (Wolanin *et al.*, 2015a; Joiner & Vasilkov, 2006). Spatial resolution of atmospheric sensors has advanced. TROPOMI sets a new record in spatial resolution with 3.5 km by 5.5 km (3.5 km by 5.5 km until 5 Aug 2019) and correspondingly this is the resolution of TROPOMI level-1 and level-2 products.

The S5POC project exploited TROPOMI's potential for retrieving ocean color products. This helps not only for obtaining hyperspectrally-derived ocean color data sets in time periods where no hyperspectral ocean color missions are available and adds understanding for hyperspectral ocean color retrievals, but also offers unique ocean color retrievals by exploiting the filling-in of Fraunhofer structures by vibrational Raman scattering (VRS) which requires a spectral resolution below 1 nm. Within S5POC-PAL the algorithm developed within S5POC for the diffuse attenuation coefficients (K_d) in the UV-AB, UV-A and short blue wavelength range by (Oelker *et al.*, 2022) is implemented and is described in detail within this document. The retrieval is based on the Differential Optical Absorption Spectroscopy (DOAS) in combination with radiative transfer modeling (RTM). S5p K_d TROPOMI products are produced at TROPOMI's level-1 and level-2 product resolution.

3.1 Introducing diffuse attenuation

The diffuse attenuation coefficient (K_d) is important for understanding biogeochemical processes and the heat budget of the global ocean. It describes how fast the incoming radiation diminishes with ocean depth z and can be calculated as a mean value over distant depths z_1 and z_2 from the change in downwelling irradiance $E_d(z)$ (Lee *et al.*, 2005a)

$$K_d(z_1 \longleftrightarrow z_2, \lambda) = \frac{1}{z_2 - z_1} \ln\left(\frac{E_d(z_1, \lambda)}{E_d(z_2, \lambda)}\right). \qquad (1)$$

which gives $K_d(z_{90}, \lambda) = 1/z_{90}(\lambda)$ for the attenuation depth z_{90} defined as the depth at which the downwelling irradiance has reduced to 1/e of its subsurface value (Gordon & McCluney, 1975).

In principle, three approaches exist to estimate K_d from multispectral ocean color sensors, two empirical and one semi-analytical. The direct one-step empirical method determines K_d from the empirical relationship between K_d and the ratio of water-leaving radiances at two wavelengths in the blue and the green (Austin & Petzold, 1981). The two-step empirical approach first determines Chla from remote sensing reflectance using a standard ocean color retrieval (O'Reilly *et al.*, 1998) and then evaluates K_d using another set of empirical relationships (Morel, 1988; Morel & Maritorena, 2001). A more recent publication presents a combination of the two empirical approaches based on ratios of water-leaving reflectances using Chla as an implicit intermediary (Morel *et al.*, 2007b). The third approach first determines inherent optical properties (IOPs), i.e., absorption and backscattering, via a quasi-analytical approach in a first step and then relates these to K_d using a LUT established through extensive radiative transfer modeling (Lee *et al.*, 2005a).

The K_d retrieval in the S5POC project is based on the work by Dinter *et al.* (2015) and Oelker *et al.* (2019) and details on the method, retrieval results and their validation and uncertainties can be found in the publication Oelker *et al.* (2022). K_d is determined from the VRS signal at the top of atmosphere. VRS occurs in liquid water when vibrational modes of the water molecules are excited by inelastic scattering with photons. Incoming radiation at a single wavelength is shifted in this process and emitted as a broad band at longer wavelengths (Stokes line). Anti-Stokes line is not considered. The mean shift from excitation to emission can be described as a constant change in wave number of around $\Delta\nu = 3357\,\text{cm}^{-1}$ with a width of the broad band emission of 821 cm^{-1} (Walrafen, 1967). VRS leads to filling-in of Fraunhofer lines, which can be detected as pseudo-absorption in backscattered radiances measured by hyperspectral satellites using DOAS (Vountas *et al.*, 2003). Dinter *et al.* (2015) found a relationship between the VRS at the top of atmosphere and the light availability or the diffuse attenuation coefficient in the ocean. In general, there is a close relationship between the number of inelastic scattering processes and the number of photons in the ocean and so the amount of light. RTM simulations are made of underwater radiant fluxes used to calculate K_d for a given scenario and of top of atmosphere radiances used to determine the VRS signal for a given scenario. RTM results are combined in a LUT relating K_d to VRS DOAS output. VRS DOAS results are then converted to K_d using satellite viewing geometry as additional input parameters in the LUT.

K_d is derived in three spectral regions: in the blue from 390 nm to 423 nm, in the UV-A from 356.5 nm to 390 nm (UVA), and in the UV-A from 312.5 nm to 338.5 nm (UVAB). These spectral regions correspond for K_d-blue to a blue DOAS fit window (450 nm to 493 nm) which has already been used in Losa *et al.* (2017) and Oelker *et al.* (2019) and for K_d-UVAB to a UV DOAS fit window (349.5 nm to 382 nm) already used in Vountas et al. Vountas *et al.* (2003, 2007). Extending the UV DOAS fit window to 395 nm was also tested to fully exploit the longer wavelengths available in band 3. However, fit results are more stable for the shorter wavelength window (until 382 nm). The K_d-UVA corresponds to a fit window from 405 nm to 450 nm (short-blue) which is tested for the first time. RTM settings closely follow Oelker *et al.* (2019), however, a more realistic atmosphere including more trace gases is used.

4 Algorithms for S5POC level-2 products

4.1 Cloud Screening

Clouds shield the radiance signal from the ocean, so the TROPOMI data set was filtered for cloud-free scenes using a cloud fraction of 0.01 as threshold. Cloud fractions were taken from the FRESCO type cloud retrieval in the nitrogen dioxide fit window (van Geffen *et al.*, 2019). Pixels over land and inland waters were removed from the data set, but are contained in the L2 products and flagged accordingly, see S5POC-PUM (Bracher & Bellido Rosas, 2024) for details.

4.2 Differential Optical Absorption Spectroscopy

Differential Optical Absorption Spectroscopy (DOAS) is a technique commonly used for the retrieval of atmospheric trace gases by distinguishing their high frequency absorption features (Perner & Platt, 1979). The DOAS method has been extended for investigating oceanic variables (PhytoDOAS). The amount of VRS (Vountas *et al.*, 2007), light availability (Dinter *et al.*, 2015) and K_d (Oelker *et al.*, 2019), Chla of different PFTs (Bracher *et al.*, 2009; Sadeghi *et al.*, 2012) and sun induced marine Chla fluorescence (SIF-marine) (Wolanin *et al.*, 2015a) have been successfully retrieved from SCIAMACHY and partly (SIF-marine and K_d) from OMI and/or GOME-2 measurements.

DOAS is based on Beer-Lambert's law. The PhytoDOAS approach can be formulated as:

$$\begin{aligned}\tau(\lambda) &= \ln(I_0/I) \\ &= \sum_{i=1}^{I} S_{a,i}\sigma_{a,i}(\lambda) + \sum_{j=1}^{J} S_{p,j}\sigma_{p,j}(\lambda) + \sum_{k=1}^{K} S_{s,k}\sigma_{s,k} + S_R\sigma_R \\ &- \sum_{l=1}^{L} S_{e,l}\sigma_{e,l} + \sum_{m=0}^{M} x_m\lambda^m \end{aligned} \tag{2}$$

where τ is the optical depth calculated as the natural logarithm of the solar irradiance I_0 and the backscattered radiance I measured by the satellite. The optical depth is a sum of all contributions from constituents in the atmosphere and ocean that modify the intensity by scattering or absorption. Absorption in the atmosphere is accounted for by a sum over I atmospheric absorbers with an optical depth calculated as product of slant column density $S_{a,i}$ and absorption cross section $\sigma_{a,i}$. The slant column density is the number density of the absorber integrated along the effective light path through the atmosphere. Likewise, $S_{p,j}$ are the slant columns or scaling factors of J oceanic absorbers with absorption cross sections $\sigma_{p,j}$. Inelastic scattering effects in the ocean are described by scaling factors $S_{s,k}$ and inelastic reference spectra $\sigma_{s,k}$. Atmospheric inelastic scattering is known as the Ring effect caused by rotational Raman scattering (RRS). S_R and σ_R are the scaling factor and reference spectrum for the Ring effect, respectively. Instrumental effects caused, e.g. by straylight in the instrument, can also be included using reference spectra $\sigma_{e,l}$ that characterize the spectral structure of, e.g. the straylight. $S_{e,l}$ are the corresponding scaling factors. A low order polynomial, typically $M < 5$, is added to account for all broad band effects such as elastic scattering in atmosphere and ocean and colored dissolved organic matter (CDOM) and non-algae particle absorption in the ocean. Eq. 2 is solved by Levenberg Marquardt least squares minimization solving for the various scaling or fit factors S and the polynomial coefficients x_m.

Inelastic scattering processes lead to filling-in of Fraunhofer lines. They are treated as pseudo-absorbers in DOAS, with their reference spectra calculated from RTM radiances including I^+ and excluding inelastic processes I^-:

$$\sigma_s = \ln \frac{I^+}{I^-} \tag{3}$$

In the atmosphere as well as in the ocean, inelastic scattering processes are present. In the ocean, fluorescence and VRS are the two important processes. The later was investigated for the retrieval of K_d products within the S5POC project.

The DOAS method can be used in small, only a few nanometer wide, wavelength windows, but also in larger wavelength windows, tens of nanometer wide, depending on the target. Only absorbing constituents and scattering processes relevant in these wavelength windows have to be considered in the DOAS fit.

The scaling or fit factors obtained for the target constituent have to be converted into a physical value, e.g. Chla. This conversion is done with the help of LUTs based on RTM simulations.

4.3 Radiative transfer model simulations

The ocean-atmosphere coupled RTM SCIATRAN (Blum *et al.*, 2012; Rozanov *et al.*, 2014, 2017) version 4.0.8 is used for simulations which are used for calculating reference spectra and LUTs and evaluating retrieval sensitivity. The optical properties of the ocean are varied by changing the Chla (case 1 waters). Other optically active constituents such as CDOM change proportionally. Top of Atmosphere (TOA) radiances are modeled for 23 different case-1 scenarios with Chla ranging between 0 and 30 $\mathrm{mg/m^3}$. A standard case-1 model is used based on Morel & Maritorena (2001) parameterization for chlorophyll and CDOM absorption. A recent water absorption spectrum by Mason *et al.* (2016) is used. Particle scattering is implemented with a wavelength-independent Fournier-Forand phase function as in the widely used Hydrolight case-1 water model (Mobley & Sundman, 2013). A background maritime aerosol is assumed with aerosol optical depth (AOD) of 0.1 at 550 nm. Detailed model settings can be found in Oelker *et al.* (2022) adapted from Oelker *et al.* (2019) and Dinter *et al.* (2015).

A TROPOMI-measured extraterrestrial solar spectrum was used for the TOA radiance calculations, since spectral alignment is very important for the DOAS retrieval. A solar spectrum measurement from a middle CCD row (row 225, 0-based) from May 2018 was chosen.

Geometry settings were chosen to cover all of TROPOMI's viewing geometries, except for the azimuth angle which was held constant:

- TOA radiances were modeled for 13 different solar zenith angle (SZA, defined on ground), i.e. 5° steps between 15° and 70°.
- Viewing zenith angle (VZA) was varied between 0° and 60° in steps of 5°.
- Relative azimuth angle was set to 90°.

4.4 Diffuse attenuation coefficients

K_d is derived from VRS retrieved using the PhytoDOAS method. The average K_ds are derived in three different spectral regions 312.5 to 338.5 nm (K_d-UVAB), 356.5 to 390 nm (K_d-UVA), and 390 to 423 nm (K_d-blue). Since the wavelength is shifted in the VRS process by between 35 and 60 nm in this spectral range, the three K_ds correspond to the VRS signal in three spectral regions with longer wavelengths, i.e., 349.5 to 382 nm, 405 to 450 nm, 450 to 493 nm, respectively. Since TROPOMI K_d-blue was much higher than expected an offset correction was applied to the VRS-blue fit factors. Then K_d is derived from VRS fit factors via a LUT. Details of the algorithm steps follow below and are also published in Oelker *et al.* (2022). Figure 1 provides an overview over the K_d algorithm.

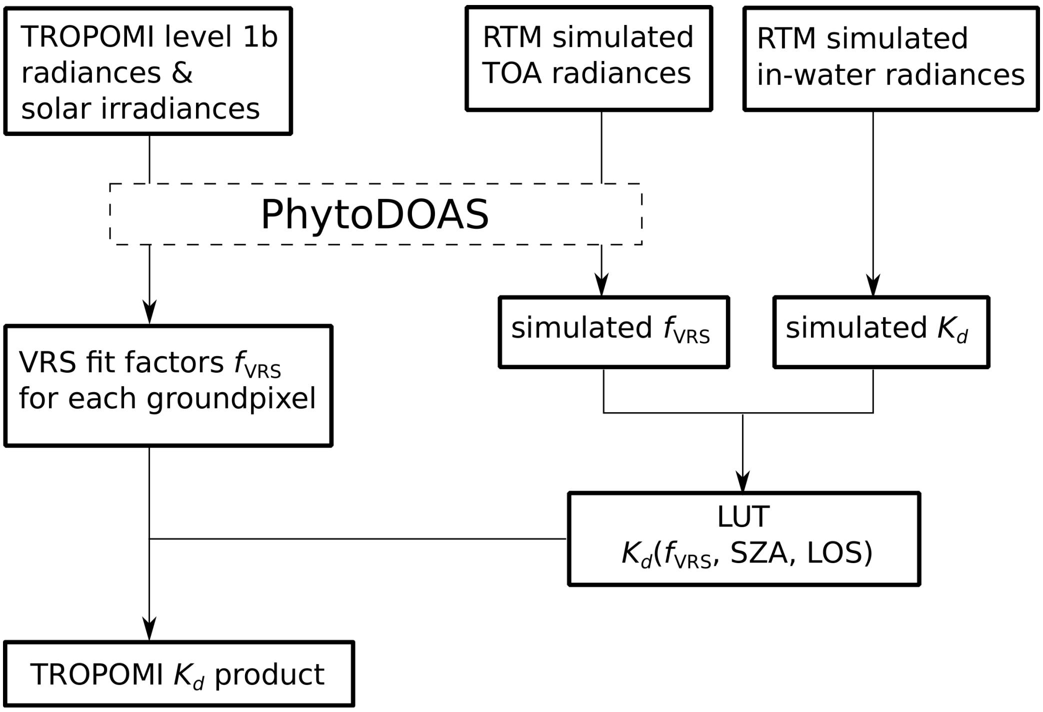

Figure 1: Flow chart illustrating the TROPOMI diffuse attenuation (K_d) algorithm. Figure from in Oelker *et al.* (2022).

4.4.1 PhytoDOAS VRS fit

Three VRS fits are performed in three spectral regions 349.5 to 382 nm, 405 to 450 nm, and 450 to 493 nm, in the following referred to as UVA, short-blue, and blue window, respectively. The short-blue and blue windows lie in band 4 of TROPOMI's spectrometer, whereas the UVA window lies in band 3. The VRS fits in the short-blue and blue window only differ in fit window, whereas the UV window fit additionally differs in the fitted atmospheric absorbers. Considering all relevant processes in these fit windows for targeting VRS, eq. 2 reduces to:

$$\tau = \ln \frac{I_0}{I} = \sum_{i=1}^{I} S_{a,i}\sigma_{a,i}(\lambda) + S_{VRS}\sigma_{VRS}(\lambda) - S_{OC}\sigma_{OC}(\lambda) - S_R\sigma_R(\lambda) + \sum_{m=0}^{M} x_m\lambda^m. \quad (4)$$

For all three fit windows, a second order polynomial was chosen $M = 2$. The following cross sections are included in the PhytoDOAS fits for all three fit windows:

- pseudo-absorption cross section for RRS (σ_R) accounting for the Ring effect Grainger & Ring (1962) in the atmosphere. RRS pseudo-absorption cross sections are calculated based on eq. 3 Vountas *et al.* (1998).
- pseudo-absorption cross sections for VRS (σ_{VRS}) that were calculated based on eq. 3 from modeled case I TOA radiances for a Chla of 0.1 mg/m^3 and a SZA of 40°.
- ocean weighting function (σ_{OC}) defined as in Dinter *et al.* (2015) calculated from case-1 TOA radiances for a SZA of 40°. The weighting function was calculated for a change in Chla from 0.1 mg/m^3 to 0.11 mg/m^3.

Changes in SZA and Chla lead to spectral distortion of the reference spectra. Reference spectra were calculated for conditions (SZA and Chla) that lie in the middle of the ranges encountered for satellite images. Using these average conditions for calculating the spectra ensures that there is a large regime where fit factor and Chla are linearly related. Figure 2 shows the ocean weighting function and VRS reference spectrum.

For the blue and short-blue window, following atmospheric absorbers were fitted: absorption cross sections for ozone (O_3, Serdyuchenko *et al.*, 2014), nitrogen dioxide (NO_2, Vandaele *et al.*, 1998), water vapour (H_2O, Rothman *et al.*, 2013 using HITRAN 2009), oxygen dimer (O_4, Thalman & Volkamer, 2013). In the UVA window, the absorption cross section for bromine monoxide (BrO) was additionally fitted, but water vapour was removed from the list of absorbers.

Figure 3 shows an example of the differential optical depth for VRS, the ocean weighting function (second and third term in equation 4, respectively) and the VRS fit residual when the PhytoDOAS retrieval was applied to a TROPOMI ground pixel in the South Atlantic Gyre in the UV wavelength region. As expected for this region a strong VRS signal is obtained with the fit residual showing

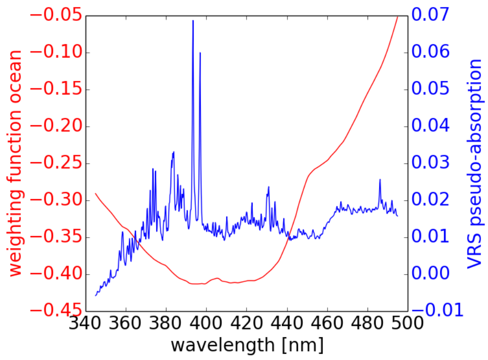

Figure 2: Ocean weighting function (red) and VRS reference spectrum (blue) as function of wavelength. Figure adapted from Oelker *et al.* (2022).

about 10% of this magnitude. Also the ocean weighting function is well fitted with similar order of residual values. Similarly good fit results are obtained for the same pixel for the VRS fit in the short-blue and blue (see Figure 4). This indicates that the signals from VRS and other ocean parameters are detected very well by the DOAS fit in the TOA radiances.

4.4.2 Radiative transfer simulations for VRS conversion to K_d

Two types of RTM simulations have to be performed for converting VRS fit factors to K_d. On the one hand TOA radiances and on the other hand underwater radiant fluxes for various case I ocean scenarios are needed. The model should accurately describe radiative transfer processes, especially inelastic processes, in the atmosphere and in the ocean at high spectral resolution matching the spectral resolution of the satellites of about half a nanometer. The theoretical description of VRS is based on the formulation of VRS by Haltrin & Kattawar (1993). The reverse process (Anti-Stokes line) where a photon gains energy in the scattering event is much less likely in nature, since most molecules occupy the ground state. It is therefore neglected in the SCIATRAN model. Correct implementation of VRS in SCIATRAN was evaluated by comparison with other radiative transfer models and experimental data from satellite, ship-based, and underwater instruments (Rozanov *et al.*, 2017). To calculate the TOA radiances, RTM settings are chosen as described in section 4.3. Modeled TOA radiances are used to calculate VRS pseudo-absorption cross sections (eq. 3) and to perform comparative DOAS retrievals for building a LUT. Underwater fluxes are used to calculate K_d for a given model scenario. Underwater fluxes were simulated at a spectral resolution of 0.5 nm using a Fraunhofer atlas (Chance & Kurucz, 2010) since they are insensitive to the exact spectral resolution. Other model

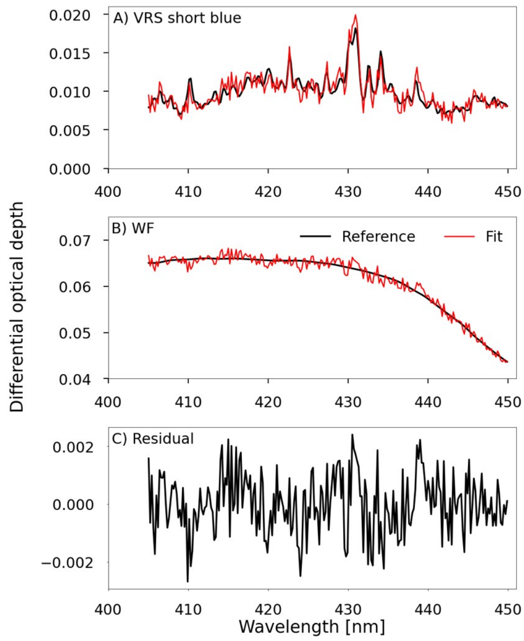

Figure 3: Differential optical depth for VRS, other oceanic parameters (oceanic weighting function - WF) and residual of the spectral fit of TROPOMI TOA radiances using DOAS for the short-blue (405-450 nm) wavelength range for one pixel measured on 11 May 2018 at 16:02:37, 29.09°W, 32.12°S, at 59.56° SZA. For plots A) and B), the black line shows as reference the differential cross section multiplied by the retrieval fit factor for the corresponding ground pixel and the red line the reference plus the overall fit residual. Figure adapted from Oelker *et al.* (2022).

settings are the same as for the TOA radiances (section 4.3). Figure 5 illustrates simulated spectra. Figure 5 a) shows the differential optical depth as calculated from the simulated TOA radiances for different Chla. A second order polynomial was fitted to τ and subtracted. Simulated underwater fluxes are depicted in Figure 5 b) as a function of wavelength for different Chla. Figure 5 c) shows the VRS fit factors obtained with DOAS fit on these simulated differential optical depths as a function of Chla for different SZAs. The K_d averaged over the blue spectral range is shown as a function of Chla in Figure 5 d).

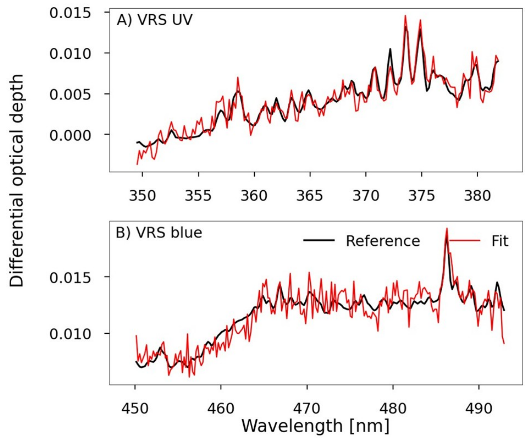

Figure 4: Differential optical depth for VRS of the spectral fit of TROPOMI TOA radiances using DOAS for the UV (349.5 to 382 nm), (A), and blue (450 to 493 nm), (B), wavelength range for one pixel of TRPOMI data measured at 11 May 2018 on 16:02:37, 29.09°W, 32.12°S. at 59.56° SZA. The black line shows as reference the differential cross section multiplied by the retrieval fit factor for the corresponding ground pixel and the red line the reference plus the overall fit residual. Figure adapted from Oelker *et al.* (2022).

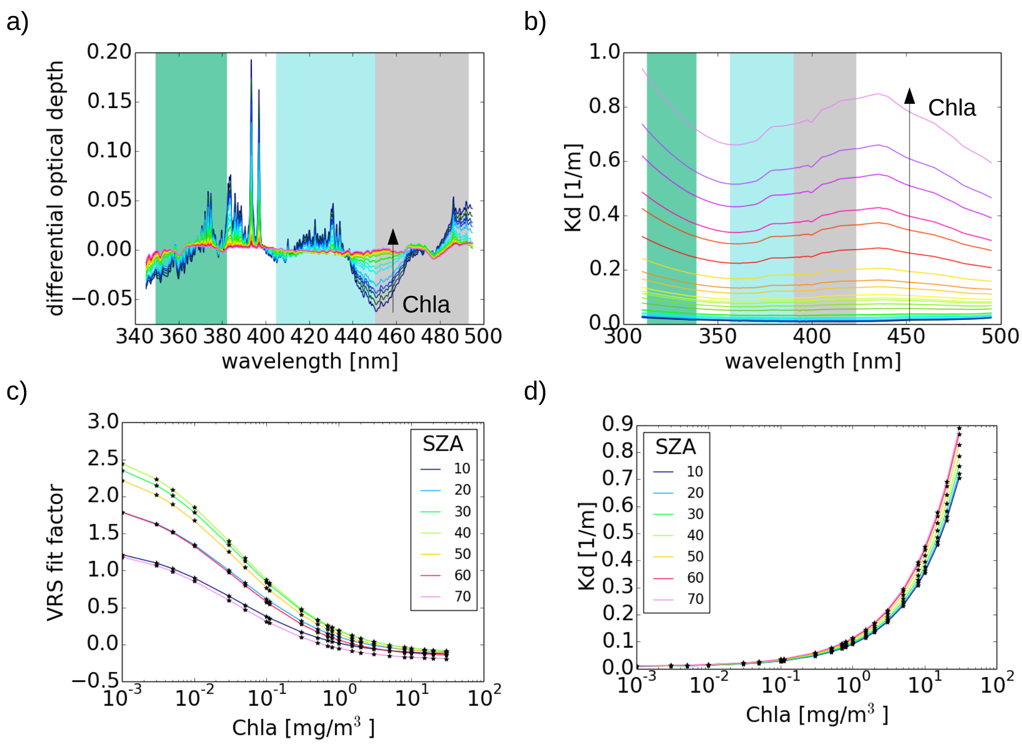

Figure 5: a) Differential optical depth as a function of wavelength for different Chla and SZA $= 40°$ calculated from simulated TOA radiances and model-input irradiance by subtracting second order polynomial. Colored areas indicate the DOAS fit window in the blue (grey, 450-493 nm), shortblue (blue, 405-450 nm), and UV (green, 349.5-382 nm) for deriving K_d-blue, -UVA, and -UVAB, respectively. b) Spectral K_d calculated from simulated underwater fluxes for different Chla and SZA $= 40°$. Colored areas indicate VRS excitation range over which

4.4.3 LUT for deriving K_d from VRS

The LUT for deriving K_d from VRS is built by combining VRS PhytoDOAS fits on simulated TOA radiances with K_d calculated from simulated underwater radiant fluxes.

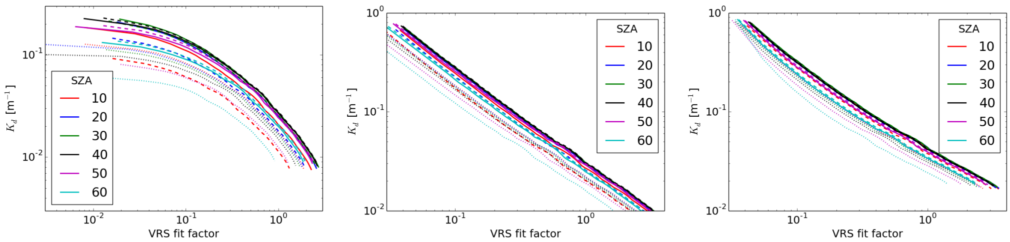

(a) (b) (c)

Figure 6: Look-up tables for converting VRS fit factors into diffuse attenuation coefficients for three spectral regions (a) blue, (b) UVA, and (c) UVAB. SZA are shown as colors. The linestyle indicates the different VZA: dashed - 0°, solid - 20°, dash-dotted - 40°, dotted - 60°.Figure from Oelker *et al.* (2022), suppl. material.

DOAS fit settings for the retrieval of theoretical VRS fit factors from the modeled TOA radiances are the same as for the retrieval on satellite radiances (see section 4.4.1) except for atmospheric cross sections. Water vapour is not fitted, since it is not included in the SCIATRAN simulation. K_d is calculated according to eq. 1 for each wavelength from the underwater radiant flux simulations which give amongst others the downwelling irradiance at discrete depths z. z_{90} is determined via linear interpolation of the log-transformed downwelling irradiance E_d at depth. Resulting K_d are then averaged over wavelength between 312.5 nm and 338.5 nm for the K_d-UVAB, between 356.5 nm and 390 nm for the K_d-UVA, and between 390 nm and 423 nm for the K_d-blue. K_d calculations and VRS PhytoDOAS retrievals are performed for each SZA and each VZA separately.

VRS fit factors are matched with K_d calculated from scenarios with the same Chla (combination of Figures 5 c) and d)). A three-dimensional LUT is created where K_d is a function of VRS fit factor, SZA, and VZA. LUTs for K_d in the three spectral regions from the blue to the UV are shown in Figure 6. Only every second SZA and every fourth VZA from the range of all simulated angles are shown.

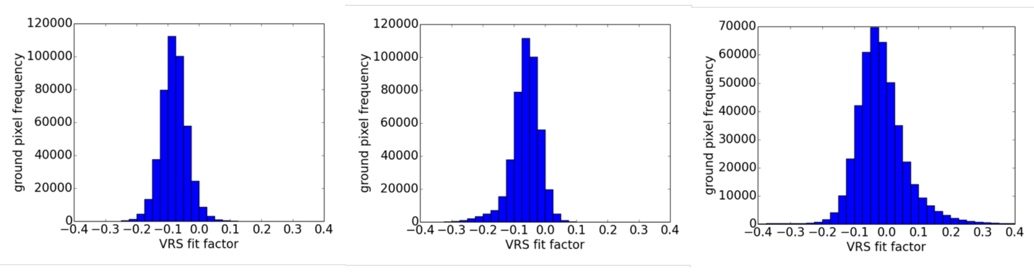

Figure 7: TROPOMI VRS-fit factor frequency distributions for the three wavelength windows (from left to right) UVA, short-blue and blue over cloudy scenes for 14 to 20 May 2018 in the Atlantic Ocean.

4.4.4 TROPOMI processing to VRS and Kd

TROPOMI level-1b data of the time period 11 May to 9 June 2018 obtained over the Atlantic Ocean were processed (see section 4.4.1) for the three PhytoDOAS fit windows in the UV, short-blue and blue to retrieve VRS fit factors. Additionally, for investigating instrumental effects on the VRS retrievals, VRS fit factors of completely cloudy scenes were analysed. The fit factors for VRS at the three wavelengths windows (UVA, short blue and blue) were zero or very close to zero (Figure 7), which indicates that the influence of instrumental effects on the retrieval is small, opposed to GOME-2 VRS-fits, for which a large VZA dependence was found over clouds (see Oelker (2021)).

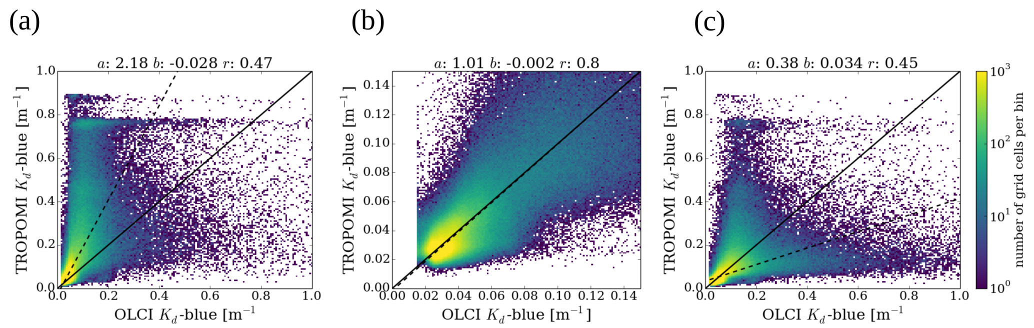

Figure 8: K_d-blue derived from a) original and offset corrected (b, c) TROPOMI VRS fit factors versus daily matchups of OLCI K_d-blue (for details on this products see S5POC-VR) for 11 May to 9 June 2018, both gridded at 0.083° for 11 May to 9 June 2018 and the Atlantic Ocean. Figure from Oelker *et al.* (2022), suppl. material.

After applying the LUT as described in section 4.4.3, TROPOMI-derived K_d-blue was much higher than expected (see comparisons to K_d from in-situ and to similar satellite products in S5POC-VR, see Figure 8a). Figure 9 shows the originally retrieved VRS-blue and K_d-blue for this time period and area. Therefore, an empirical offset correction had to be developed which improved the agreement of K_d-blue to the wavelength-converted $K_d(490)$ from OLCI and OC-CCI when a constant was added to the VRS fit factors. Generally, TROPOMI original K_d-blue is closer to the OLCI K_d-blue than the OC-CCI K_d-blue and correlation is highest for low K_d values (see Table 5 and Figure 5 in S5POC-VR).

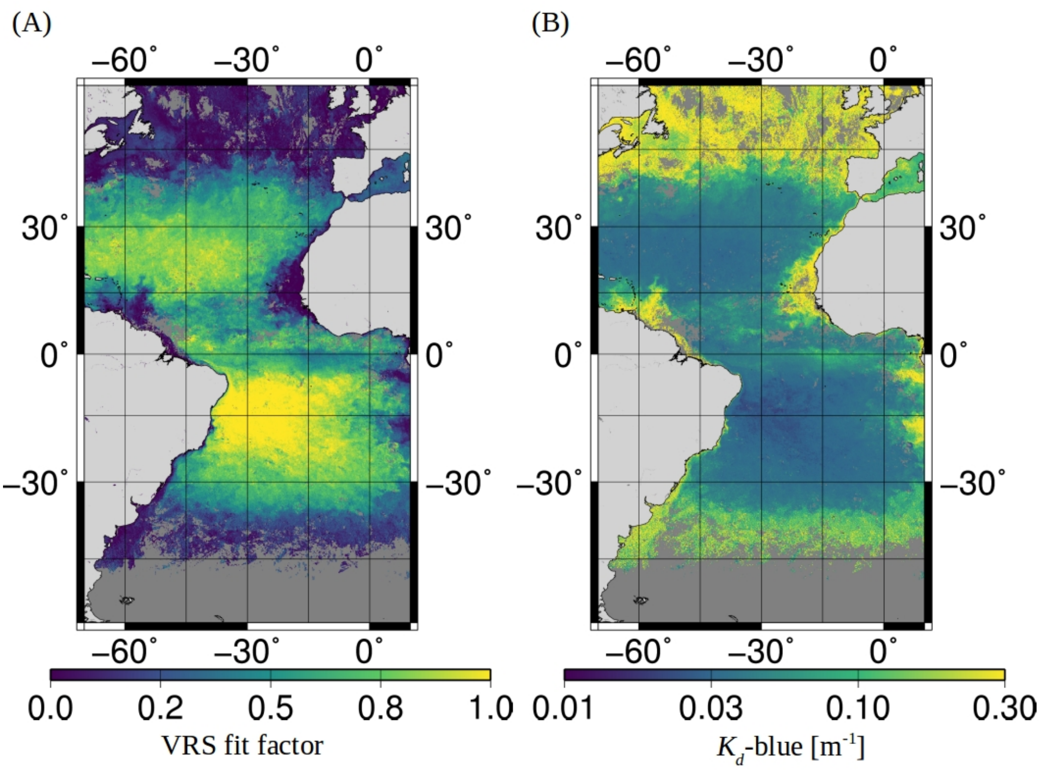

Figure 9: Original TROPOMI VRS fit factors (left) and correspondingly derived K_d-blue, both gridded at 0.083° as mean for 11 May to 9 June 2018 for the Atlantic Ocean. Figure from Oelker *et al.* (2022), suppl. material.

Therefore, the offset correction applied to the input VRS-blue data for the LUT was derived from comparing the low values (K_d <0.15 m^{-1}) of TROPOMI K_d-blue to those from the OLCI K_d-blue data set to determine the offset for VRS-blue that best corrects the data. This was based on considering daily 5 min gridded matchup K_d-blue data from TROPOMI and OLCI within the entire RV Polarstern expedition PS113 time period (11 May to 9 June 2018) and area of 50°S to 50°N and 70°W to 10°E. The offset correction was optimized such that a linear total-least square regression on this restricted comparison data set yielded a slope close to one. The optimal offset to VRS-blue fit factor was found to be 0.186. Regression statistics for using this setting to derive the final K_d-blue resulted in the comparison to OLCI K_d-blue in a slope of 1.01, an intercept of -0.002 m^{-1}, and a Pearson correlation coefficient of 0.80 (Figure 8b) for this restricted data set. The offset was used to correct all VRS fit factors, also retrieved for regions D, and by that the whole K_d-blue range (Figure 8c).

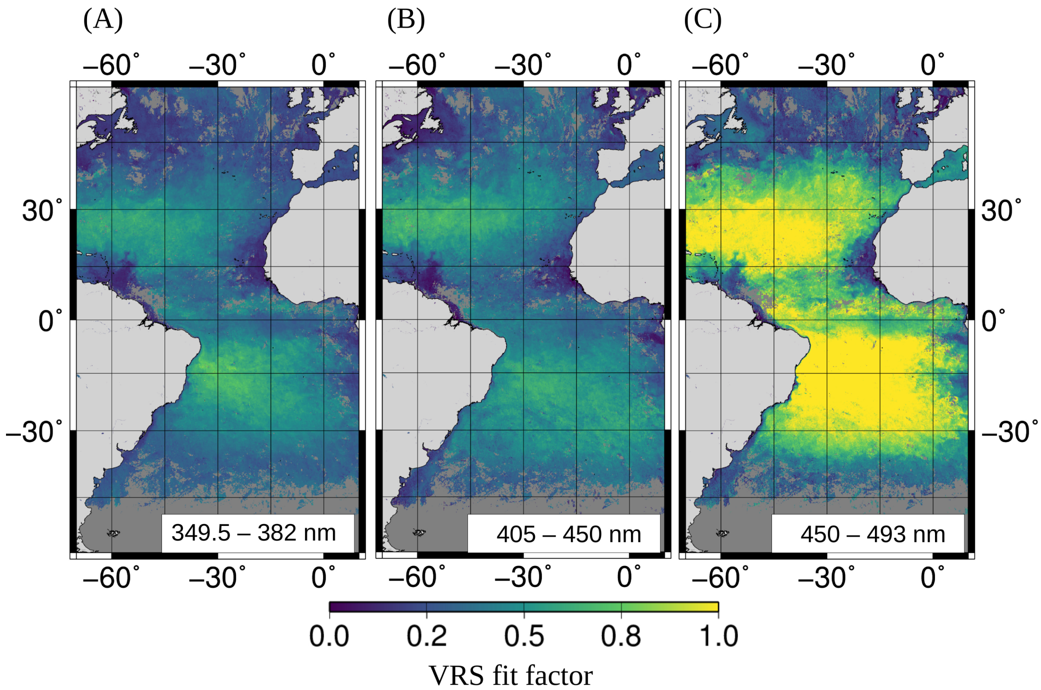

Figure 10: TROPOMI VRS fit factors in the (from left to right) UVA, short-blue and blue fit window in the Atlantic Ocean for 11 May to 9 Jun 2018. For TROPOMI VRS-blue fit factors an offset of 0.186 was added to the original VRS-blue (Figure 9). Figure from Oelker *et al.* (2022).

Figure 10 shows VRS fit factors retrieved from TROPOMI level-1b data for the three PhytoDOAS fit windows in the UV, short-blue and blue for the same time period and area as described above. VRS-blue fit factors are offset corrected. For all three fit windows, high and low VRS fit factors are found in typically low and high Chla corresponding to low and high light penetration into the ocean, respectively. As expected, the VRS signal increases with increasing wavelength window. The average root mean square (RMS) of all fit residuals in this area and time period and its standard deviation were evaluated to $1.0 \cdot 10^{-3} \pm 3 \cdot 10^{-4}$ for the UV (excluding 26 outliers with RMS >4), $0.9 \cdot 10^{-3} \pm 2 \cdot 10^{-4}$ for the short-blue, and $1.0 \cdot 10^{-3} \pm 3 \cdot 10^{-4}$ for the blue fit window. VRS fit factors from different fit windows are not strictly correlated, e.g., differences

564 appear around Newfoundland and Great Britain.

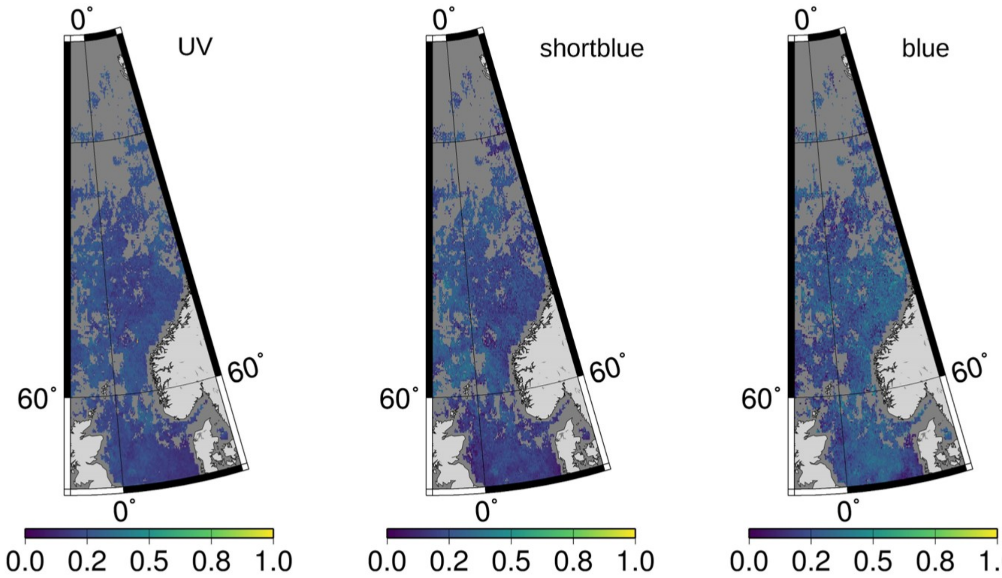

Figure 11: TROPOMI VRS fit factors (from left to right) UVA, short-blue and blue fit window for 11 Aug to 10 Sep 2019 for the North Sea up to the Fram Strait. For TROPOMI VRS-blue fit factors an offset of 0.186 was added. Pixels with SZA $>$ 70°were screened out, because 70° is the largest SZA in the LUT.

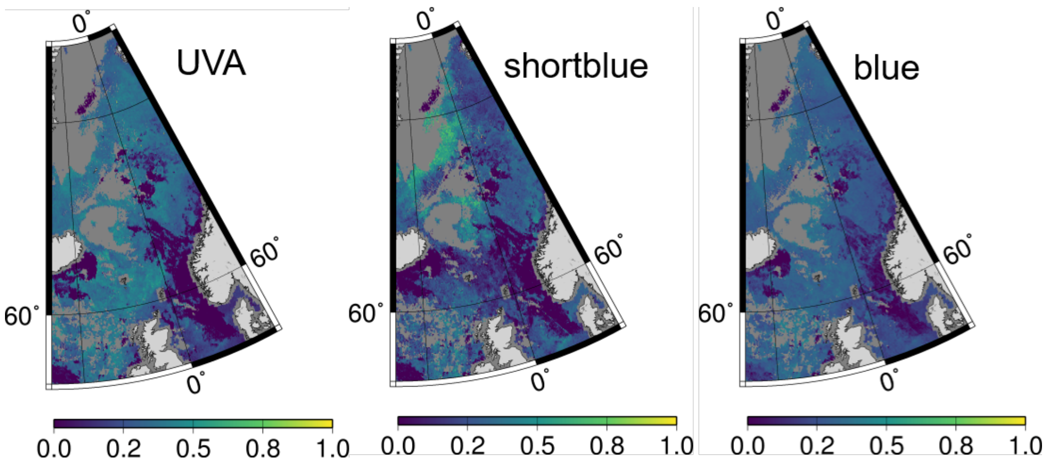

Figure 12: TROPOMI VRS fit factors (from left to right) UVA, short-blue and blue fit window for 27 Jun to 25 Jul 2020 for the North Sea up to the Fram Strait, including East Greenland waters. For TROPOMI VRS-blue fit factors, an offset of 0.186 was added. Pixels with SZA $>$ 70°were screened out, because 70° is the largest SZA in the LUT.

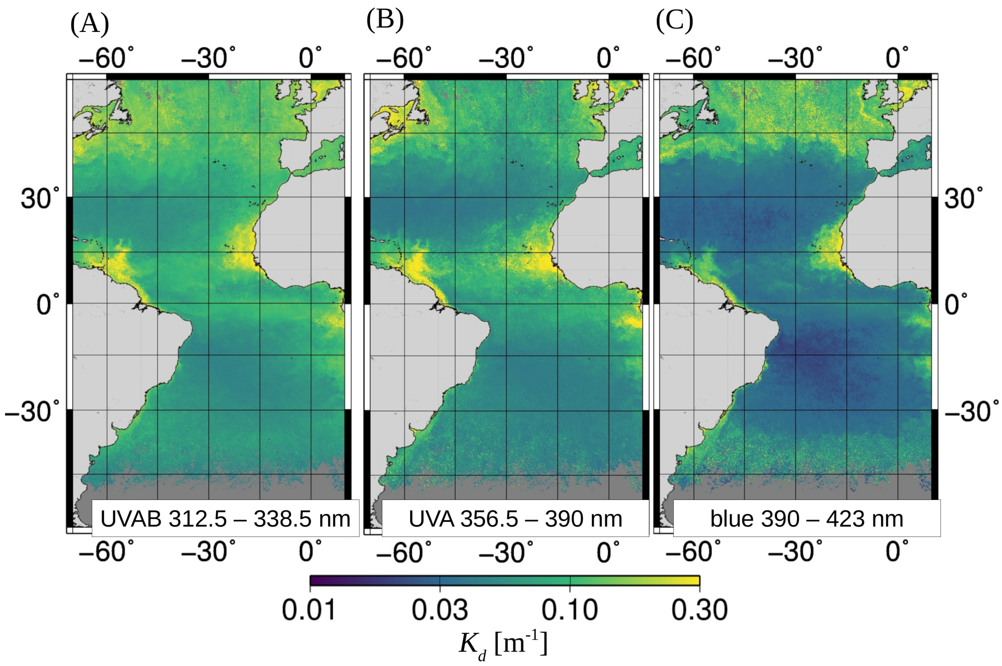

Figure 13: TROPOMI (A) K_d-UVAB, (B) K_d-UVA, and (C) K_d-blue gridded at 0.083° as mean for 11 May to 9 June 2018 for the Atlantic Ocean. Figure from Oelker *et al.* (2022).

TROPOMI K_d was derived from the VRS fit factors, shown in Figure 10, Figure 11 and Figure 12, using the separate LUTs (as described in section 4.4.3) for each wavelength region. In Figure 13 the resulting (A) K_d-UVAB, (B) K_d-UVA, and (C) K_d-blue in the Atlantic Ocean for the PS113 (for region D, see Fig. 4 in S5POC-VR) can be seen for the same time period. Lowest K_d are found in the North and South Atlantic Gyres, highest K_d in the upwelling regions along the African coast and the Amazon river plume. With decreasing wavelength, K_d increases. However, K_d-UVAB is not generally larger than K_d-UVA. In upwelling regions off the coast of West Africa, the Amazon river plume, around Newfoundland, and around Great Britain, the ratio K_d-UVA/K_d-UVAB is larger than 1 (roughly 1.25 on average, 2 in extreme cases). Similarly in 2020 in the North Atlantic K_d-UVA is significantly higher even outcompeting K_d-blue. K_d-blue is much lower in the subtropical and tropical ocean and shows values between K_d-UVA and UVAB in the productive areas north of the North Atlantic Gyre.

5 Feasibility

5.1 S5POC level-2 products

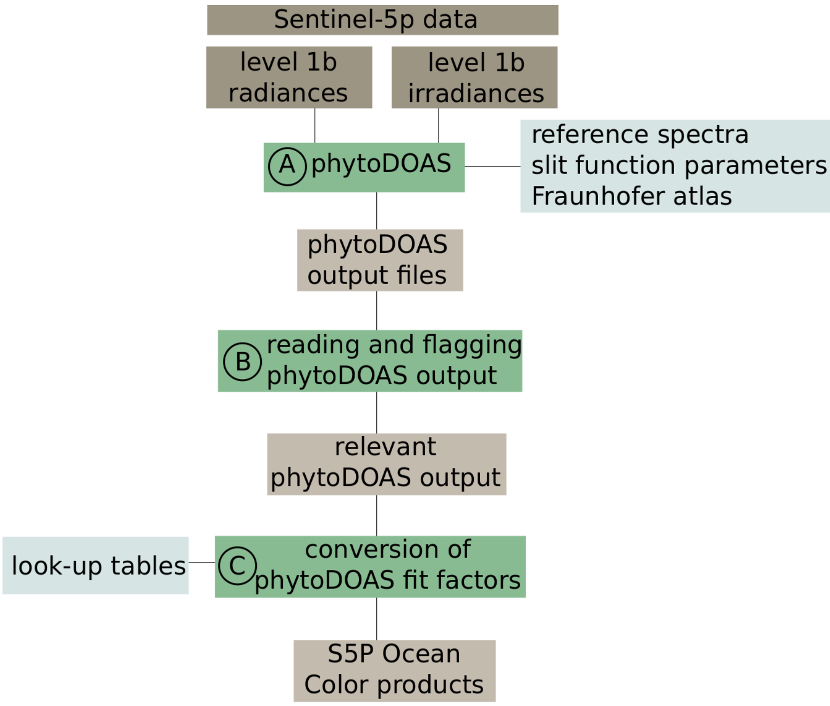

Figure 14: Scheme of the processing chain. Dynamic input files are shown in dark brown, intermediate and product files in light brown. Static input files are highlighted in grey. Processing steps A to C are shown in green.

Figure 14 schematically shows the processing chain of the TROPOMI K_d-UVAB, K_d-UVA, and K_d-blue retrievals. Dynamic input files are shown in dark grey, intermediate and output files in light grey, and static input files in light blue. The chain consists of three processing steps A, B, and C highlighted in green.

5.2 Computational effort

Processing one full orbit of TROPOMI data for all three targets (K_d-UVAB, K_d-UVA, and K_d-blue) takes roughly 7.5 minutes for step A, 1 minute for step B, and 30 seconds for step C. Through introducing parallel computing on the super computer used, 200 orbits at the same time can be processed which enables to process a whole year for the three targets in less than 4 hours. In summary, the computational load of this product is low and the output file size similar to other S5p L2 products.

6 Input Output Data Definition

6.1 Input data

Retrieval processing of Sp K_d-UVAB, K_d-UVA, and K_d-blue products requires dynamic and static input data.

6.1.1 Dynamic input

The main dynamic input data for the S5p K_d-UVAB, K_d-UVA, and K_d-blue product are TROPOMI L1 products of band 3 (for K_d-UVAB) and band 4 (for K_d-UVA, and K_d-blue) radiance and irradiance. Global data is required. In addition to the TROPOMI lv1 data, TROPOMI NO2 OFFL data are used to extract cloud information which is added to the KD L2 files.

6.1.2 Static input

Static input data for the K_d-UVAB, K_d-UVA, and K_d-blue retrieval have been presented in detail in 4.4.1 and in 4.4.3) when describing the specific retrieval steps.

They include:

Cross sections calculated from RTM (as specified in 4.4.1)

- pseudo-absorption cross sections for VRS (σ_{VRS}) that were calculated based on eq. 3 from modeled case I TOA radiances for a Chla of 0.1 mg/m^3 and a SZA of 40°.
- ocean weighting function (σ_{OC}) defined as in Dinter *et al.* (2015) calculated from case-1 TOA radiances for a SZA of 40°. The weighting function was calculated for a change in Chla from 0.1 mg/m^3 to 0.11 mg/m^3.
- pseudo-absorption cross section for RRS (σ_R) accounting for the Ring effect Grainger & Ring (1962) in the atmosphere. RRS pseudo-absorption cross sections are calculated based on eq. 3 Vountas *et al.* (1998).

Absorption cross sections available from literature (as specified in 4.4.1):

- ozone (O_3, Serdyuchenko *et al.*, 2014),
- nitrogen dioxide (NO_2, Vandaele *et al.*, 1998),
- oxygen dimer (O_4, Thalman & Volkamer, 2013)

- only for KD-UVA and KD-blue: water vapour (H_2O, Rothman *et al.*, 2013 using HITRAN 2009),
- only for KD-UVAB: bromine monoxide (BrO, Fleischmann *et al.*, 2004);

Solar Fraunhofer atlas;

LUTs (as described in section 4.4.3), separated for each wavelength region (see Figure 6).

6.2 Output Product Overview

Output data format follows the TROPOMI netcdf standard. Details on the product can be found in the S5POC-KD-PUM (Bracher & Bellido Rosas, 2024).

7 Error analysis

For S5pC K_d products their detailed assessment and total uncertainties are also provided in the publication Oelker *et al.* (2022). Uncertainties associated with S5p ocean color products were assessed through the measurement fit errors (in 7.1), the sensitivity analysis of S5POC retrievals using RTM (in 7.2), the intercomparison to ocean color products from multispectral satellite sensors and the validation with in-situ data (as in Oelker *et al.* (2022) for the temperate, subtropical and tropical Atlantic Ocean, then extended to include also the Arctic Ocean in Bracher *et al.* (2024)). Maximum errors obtained via the retrievals sensitivity studies are used as specific model errors and provided together with the measurement errors (fit errors) within the final error budget assessment (see Chapter 3 in S5POC IAR, Bracher *et al.* (2022)).

7.1 Measurement fit errors

For each TROPOMI ground pixel the fit error which is the relative uncertainty of the fit factor as determined from the linear least-squares DOAS fit, given in percent, is provided. These errors (summarized in Table 1) are lowest for VRS-UV ranging from 5 to 10$\%$, increased for VRS-short-blue to 10 to 15$\%$ and highest for VRS-blue with 15 to 20$\%$ within the given sensitivity range for the tropical and temperate Atlantic Ocean of $K_d < 0.3\,\mathrm{m}^{-1}$ (see Figure 15). Maximum errors for high K_d-/Chl-a waters are <20$\%$, <40$\%$, and <90$\%$, respectively. VRS fit factors from different fit windows are not strictly correlated, clearly showing their independencies to be retrieved reflecting the changing optical properties in the open ocean.

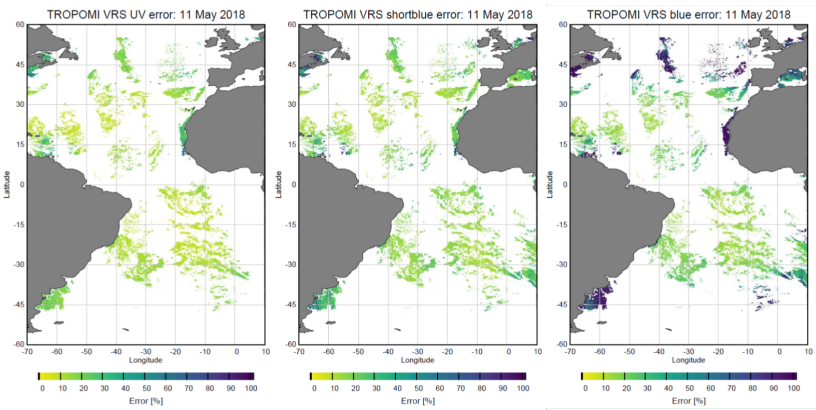

Figure 15: VRS fit errors (in percent) for 11 May 2018, same data set as shown in Figure 10.

7.2 Retrieval sensitivity

Here, we detail the results of the sensitivity analysis. Some of these results were obtained in previous studies related to similar atmospheric sensors used to obtain the same OC products (Dinter *et al.*, 2015; Wolanin *et al.*, 2015b; Oelker *et al.*, 2019). Settings in the RTM scenarios used for building the retrieval LUTs were investigated. It was tested how a change in a model parameter influences the resulting S5p ocean color product, e.g. the choice of chlorophyll-a absorption spectra in the UV region on the Kd-UVAB product. Also information on PhytoDOAS retrieval sensitivity from previous studies for estimating, e.g. the influence of vertical chlorophyll-a profile and aerosol optical depth, is included here.

The algorithm sensitivity was extending the analysis by Oelker *et al.* (2019) which focused on aerosol and CDOM settings, to the parameters: CDOM slope, UV-absorbing pigments, liquid water absorption, wind speed, and ozone concentration. For each parameter, the sensitivity was analyzed as follows. An RTM simulation was performed to calculate radiances and radiant fluxes in which one parameter is increased or decreased with respect to the standard scenario used to build the LUT as described in section 4.4.3). The PhytoDOAS fit was performed on this modified scenario. Resulting VRS fit factors were converted to K_d using the LUT. The resulting K_d, K_d^{der}, was compared to the expected K_d, K_d^{exp}, calculated from the radiant fluxes of the modified scenario. The deviation of derived from expected K_d was determined, $(K_d^{\text{der}}$ - $K_d^{\text{exp}})$ / K_d^{exp}. Since mainly only a change in inherent optical properties changes K_d, the parameters can be separated in two groups. One group comprises the atmospheric and surface parameters which have no or only a minimal effect on the mean K_d over the first optical depth, but may influence VRS since scattering is proportional to light intensity. The second group comprises the oceanic parameters which affect both, K_d and VRS. For the second group, K_d changes can be large, however, VRS changes accordingly, and K_d is retrieved correctly within an uncertainty which is only a fraction of the change in K_d.

Atmospheric and surface parameters

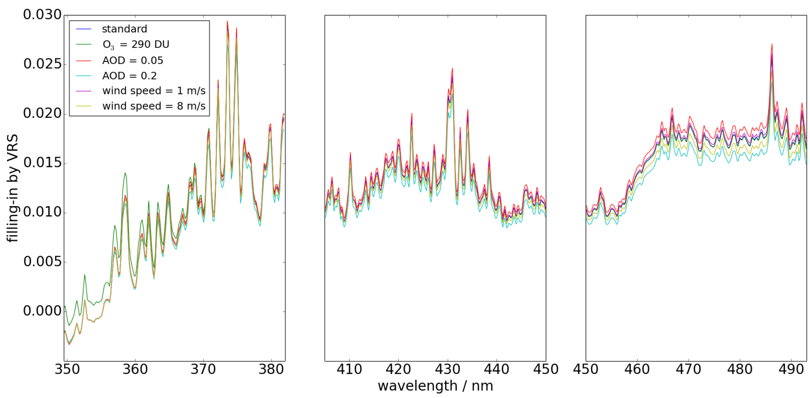

Figure 16: Filling-in by VRS for different model parameterizations in comparison to the standard simulation for the three wavelength ranges of the PhytoDOAS VRS fits. Figure from Oelker *et al.* (2022), suppl. material.

Parameters within the first group were varied as follows: wind speed was reduced to 1 m/s and increased to 8 m/s (standard: 4.1 m/s); aerosol optical depth (AOD) was reduced to 0.05 and increased to 0.2 (standard: 0.1); ozone profile was changed to one with reduced total ozone column of 290 DU (standard: 420 DU). Figure 16 shows the influence of these selected atmospheric and surface parameters on the filling-in by VRS as determined by Equation (2) in section 4.2 for Chla of 0.1mg/m3. The influence of AOD and wind speed is largest for the blue fit window and decreases with decreasing wavelength. It is negligible for wavelengths smaller 360 nm. The influence of the ozone concentration is largest at the short wavelengths. It is negligible for wavelengths larger 370 nm.

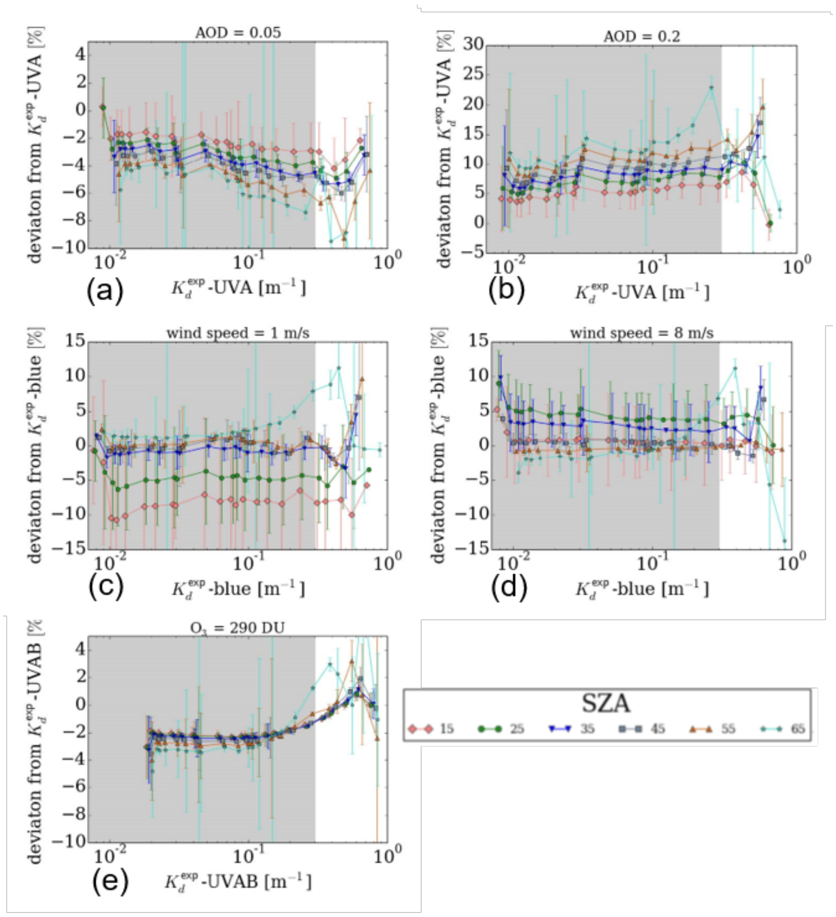

Figure 17: Deviation of derived from expected K_d in case of (a) reduced AOD, (b) increased AOD, (c) reduced wind speed, (d) increased wind speed, and (e) reduced ozone column for different SZA. Results were averaged for different VZA with the standard deviation given as error bar. (a), (b) show results for K_d-UVA, (c), (d) for K_d-blue, and (e) for K_d-UVAB. Figure from Oelker *et al.* (2022).

Results for changes in AOD and wind speed are therefore only presented for the short-blue and blue fit window and in ozone for the UV fit window. The influence of aerosols on the K_d-blue retrieval was already presented in Oelker *et al.* (2019). A constant deviation over the K_d-blue range was found which was less than -5% for the reduced AOD scenario and less than $+20\%$ for the increased AOD scenario. Figure 17 (a) and (b) show that the influence of aerosols on the K_d-UVA retrieval is similar in magnitude. The effect of aerosols on the K_d-UVAB retrieval (not shown) is significantly lower with only $+5\%$ deviation for the increased AOD scenario. Figure 17 (c) and (d) show the K_d-blue retrieval sensitivity with respect to wind speed. For most SZA, an altered wind speed causes deviations from the expected K_d-blue well below 5%. Larger deviations of up to 10% are found for specific SZA at the lower SZA range depending on wind speed. The influence on K_d-UVA was even smaller as expected from the behavior of the filling-in by VRS. For the same specific SZA, deviations up to 5% can be found (not shown). The influence of the ozone column on the K_d-UVAB retrieval is shown in Figure 17 (e) and is below 5%.

It can be seen that the retrieval performance is not robust for $K_d >$ 0.3 m^{-1} , outside of grey-shaded area in Figure 17. Later on, results will show that TROPOMI K_d can not be well retrieved for scenes with $K_d >$ 0.3 or 0.5 m^{-1} within S5POC regions C (central Atlantic) and D (Arctic Atlantic Ocean), respectively, discussed in S5POC VR. Also, the retrieval is less robust at high SZA and at high VZA, which causes large error bars in the plots. This effect should be kept in mind, when the algorithm is applied in high latitudes. In the investigated Atlantic region, SZA are only moderately high and satellite pixels with high VZA are often screened out by the cloud filter due to their larger pixel size.

In summary, the influence of atmospheric and surface parameterizations is generally low on the K_d retrievals. Uncertainties increase with the difference between conditions found for an actual satellite scene and the average ones used in the simulated standard scenario. Largest uncertainties can be expected for scenes with high aerosol loading, which only occur in specific regions and times of the year (Remer *et al.*, 2008). For the Atlantic region, Saharan dust storms can have a significant influence (e.g., van der Does *et al.*, 2016a). Maritime aerosols were investigated here, terrestrial dust might have even stronger impacts. These critical scenes are largely removed through the strict cloud filter criterion used in this study (cloud fraction of 0.01). In the future, the dimensions of the LUT can be increased, when confidence in performance of K_d retrievals has been gained by comparison with larger in-situ data sets than available for this study. The total ozone column, AOD, and wind speed can be included in the LUT and taken from ancillary data (some variables also available from TROPOMI) to further reduce uncertainty in TROPOMI K_d data sets.

Oceanic parameters

The case-1 assumption is generally not valid in the UV domain. The absorption coefficient can not be accurately described using Chla (Vasilkov *et al.*, 2002a; Morel *et al.*, 2007b). The influence of the case-1 parameterization used for the optical constituents in the ocean on the ultraviolet K_d retrievals needs to be checked carefully. As introduced in section 4.3), the case-1 parameterization for the visible wavelength range was used in combination with a recent pure water absorption spectrum accurately measured for UV wavelengths Mason *et al.* (2016). Nevertheless, the influence of the choice of water absorption spectrum was assessed. A modified scenario was simulated with liquid water absorption coefficients from Pope & Fry (1997) which significantly differ at short wavelengths from those measured by Mason *et al.* (2016), see Oelker (2021).

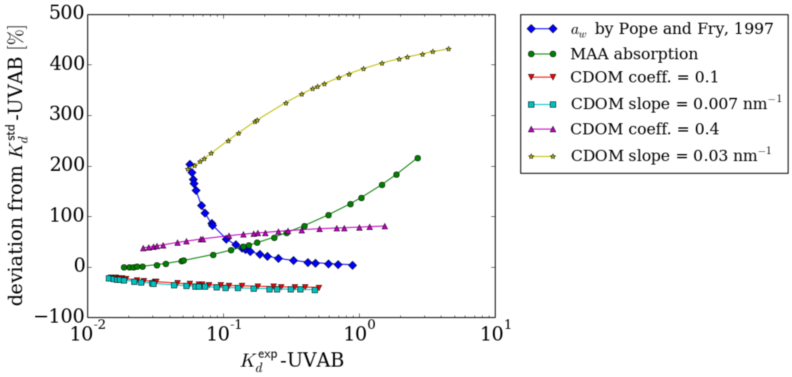

Figure 18: Deviation of K_d^{exp}-UVAB as in the modified scenario from K_d-UVAB in the standard scenario as function of K_d^{exp}-UVAB for tested variations in oceanic parameter. Figure from Oelker *et al.* (2022).

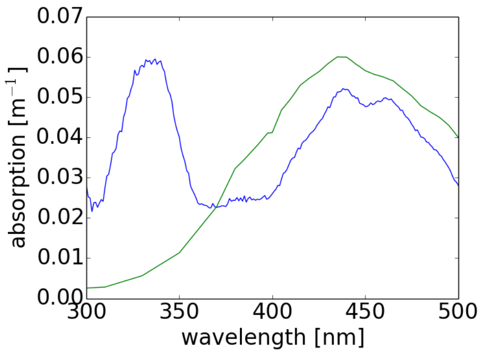

Figure 19: Phytoplankton absorption at Chla of 1 mg/m^3 in the standard (green) and in the modified (blue) simulations (S9 from Bracher & Wiencke, 2000).

High uncertainty also lies within the settings for phytoplankton and CDOM absorption. Presence of mycosporine amino acids (MAA) causes higher UV absorption than prescribed in the standard case-1 parameterization. MAA absorb between 320 and 350 nm with a peak around 330 to 340 nm (Vernet *et al.*, 1994; Bracher & Wiencke, 2000). Presence of these UV-absorbing pigments should therefore mainly influence K_d-UVAB (Wang *et al.*, 2021). In the study by Bracher & Wiencke (2000) different phytoplankton communities had been sampled in the Southern Ocean. We have further analysed these data by normalizing them to chl-a concentration. The results show that within similar phytoplankton communities the specific absorption can vary by a factor 5.2 in the UV. A modified scenario was simulated using a phytoplankton absorption spectrum with medium MAA absorption (S9 from Bracher & Wiencke (2000), see Figure 19). High variability can also be expected for the CDOM slope, 0.01 to 0.03 nm^{-1} (Vodacek *et al.*, 1997) as compared to 0.014 nm^{-1} in the standard case-1 scenario. Modified RTM simulations were made with a reduced CDOM slope of 0.007 nm^{-1} and an increased CDOM slope of 0.03 nm^{-1} . Also the CDOM coefficient was modified as in Oelker *et al.* (2019), while keeping the CDOM slope at 0.014 nm^{-1} .

Figure 18 shows the change in K_d-UVAB caused by the altered parameterizations with respect to the standard scenario (K_d^{std}), calculated as $(K_d^{\text{exp}} - K_d^{\text{std}})/K_d^{\text{std}}$. Implemented changes cause drastic changes in K_d-UVAB. The influence of the water absorption coefficients, MAA absorption, and a high CDOM slope is especially large. For the clearest waters, the water absorption by Pope & Fry (1997) leads to an increase in K_d-UVAB by 200%. A similar increase is found for MAA absorption for waters with highest Chla. Since the reference wavelength for CDOM absorption is in the visible spectral region, an increase in CDOM slope causes extreme changes in K_d-UVAB (about 200-430%). The other tested variations in CDOM parameterization lead to comparably moderate changes in K_d-UVAB below 100%.

Figure 20 shows retrieval sensitivity results for the oceanic parameters for K_d-UVAB. The focus here lies on the K_d range below 0.3 m^{-1}. The change in water absorption spectrum results in an overestimation of 15% for clear water scenarios which reduces to zero for high Chla scenarios, see Figure 20 (a). The overestimation is counter-intuitive, since ${K_d}^{\text{exp}}$ is higher than ${K_d}^{\text{std}}$. A changed parameterization often also causes a spectral change in K_d which impacts the VRS fit quality and can result in this unexpected behavior. MAA absorption leads to an underestimation which increases to 20% at K_d-UVAB $=>$ 0.3 m^{-1}. and can be significantly higher for higher K_d-UVAB (Figure 20 (b)). A change in CDOM coefficient causes deviations of $\pm 10\%$ (Figure 20 (c) and (d)). A reduced CDOM slope results in an overestimation of up to 20% and an increased CDOM slope in an underestimation of up to 30% depending on Chla as shown in Figure 20 (e) and (f). The influence on the K_d-UVA retrieval was also evaluated with respect to water absorption and CDOM (results not shown). Results are qualitatively similar, however, the influence is generally smaller. Overestimation up to 10% for the change in water absorption, overestimation of up to 10% in case of reduced CDOM slope, and underestimation up to 25% in case of increased CDOM slope are found. A change in CDOM coefficients leads to similar deviations of $\pm 10\%$.

In conclusion, the K_d-UV retrievals are rather insensitive to the chosen RTM parameterization compared to the large variability that this parameterization causes in K_d in the ultraviolet spectral range. Maximum errors of the retrieval sensitivity are summarised in Table 1 of chapter 3.1.4 in Bracher *et al.* (2022).

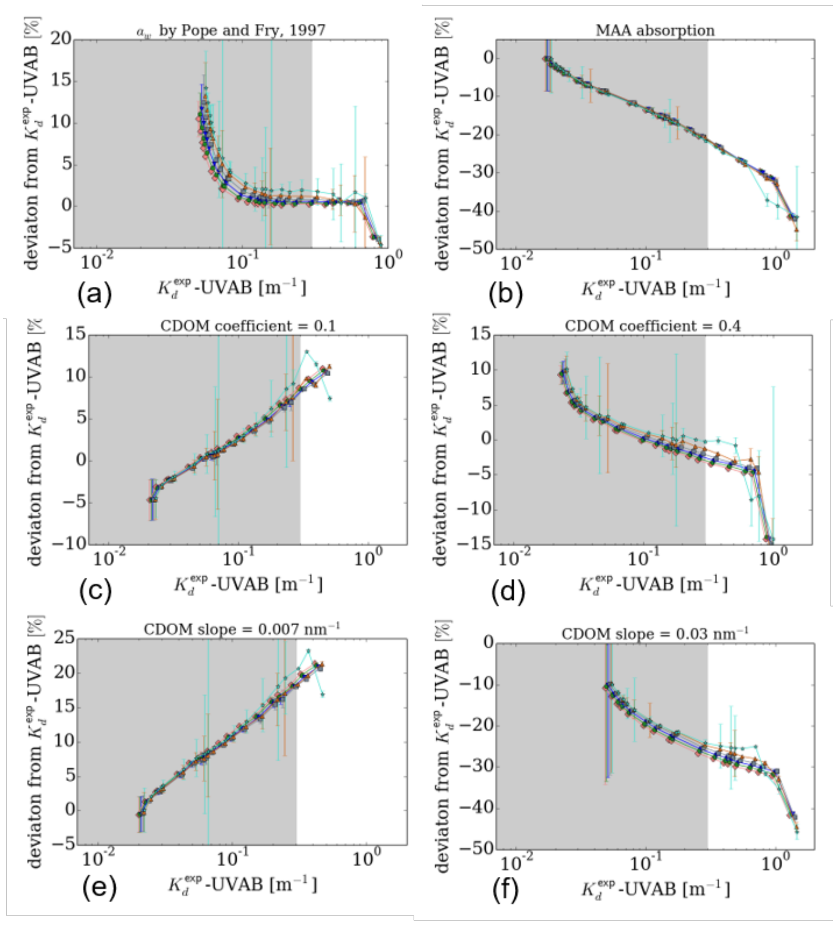

Figure 20: Deviation of derived from expected K_d-UVAB in case of (a) liquid water absorption by Pope & Fry (1997), (b) (f) MAA absorption as function of expected K_d-UVAB, (c) reduced and (d) increased CDOM coefficient, (e) reduced and (f) increased CDOM slope. Results were averaged for different VZA with the standard deviation given as error bar. See Figure 17 for symbol legend. Figure from Oelker *et al.* (2022).

7.3 S5p K_d products uncertainty

When specifying the uncertainty of the retrieved VRS fit factor and derived Kd retrievals, several effects have to be taken into account:

Photon-shot noise, related to the number of photons collected in a single measurement and governed by the probability distribution of incoming photons (Burrows *et al.*, 2011), together with readout noise and the detector's dark signal, are the main sources of random errors in the radiance measurements.

Systematic errors in the VRS fit factors are introduced by an imperfect wavelength calibration and other instrumental features not fully calibrated for in the TROPOMI Level-1 data calibration (e.g., Ludewig *et al.* (2020)) and uncertainties in the reference spectra of all considered atmospheric absorbers, RRS, VRS and oceanic weighting function. The uncertainties in the reference spectra are propagated into the conversion of the VRS fit factor into K_d. The LUTs, used for the conversion, further introduce systematic uncertainties by not fully representing atmospheric and oceanic optical properties. In addition, the presence of clouds could lead to significant uncertainties in satellite retrievals.

Within our retrieval the errors introduced by clouds can be considered as marginal as we apply a strict cloud filtering. The VRS fit factor error represents random errors listed above and also includes most of the systematic errors considering imperfect wavelength calibration, instrumental effects and uncertainties in the reference spectra. The results from the retrieval sensitivity studies (provided in section 7.2, Dinter *et al.* (2015); Oelker *et al.* (2019)) as quantitative assessment of the TROPOMI K_d uncertainty give information on the systematic errors introduced by specific settings of the parametrizations in SCIATRAN related to LUTs to convert the VRS fit factor into the K_d value which are discussed in the following.

The influence of atmospheric and surface parameterizations on the TROPOMI K_d retrievals can be considered generally low. Uncertainties increase with the difference between conditions found for an actual satellite scene and the average ones used in the simulated standard scenario. Largest uncertainties can be expected for scenes with high aerosol loadings, which only occur in specific regions and times of the year (Remer *et al.*, 2008). For the Atlantic region, Saharan dust storms can have a significant influence (e.g.,van der Does *et al.*, 2016b). Maritime aerosols were investigated here while terrestrial dust might have even stronger impacts. However, these critical scenes are largely removed through the strict cloud filter criterion used in the retrieval (cloud fraction of 0.01). We conclude that the here presented LUT presents a solid basis for K_d retrievals in the blue and UV spectral range. Compared to other semi-analytic approaches, the degree of assumptions made is similar. For instance, RTM simulations for the K_d method by Lee *et al.* (2005b) were also made for a mean global wind speed. Nevertheless, to further enhance the quality of the LUT-derived K_d in the future, the dimensionality of the LUT can be further increased to include aerosol loading, wind speed, and ozone column as input parameters that can be taken from ancillary data sets with sufficient quality. Parameters like aerosol optical depth and ozone column are even provided by the TROPOMI sensor.

With respect to the oceanic parameters, the TROPOMI K_d retrievals are rather insensitive to the chosen RTM parameterization compared to the large variability that this parameterization causes in K_d in the UV spectral range. The analysis in this study focused on the UV spectral range for two reasons: (1) the influence of oceanic parameterization on the K_d-blue was already discussed in Dinter *et al.* (2015) and Oelker *et al.* (2019) and (2) parameterization in the UV spectral range is less straight forward since a simple parameterization with Chla as used in the visible region for case I waters is not suitable (Morel *et al.*, 2007a; Vasilkov *et al.*, 2002b). As demonstrated by the sensitivity analysis, the exact oceanic RTM parameterization is not of importance since a change in oceanic parameter causes a change in K_d and VRS. The uncertainties of derived K_d for scenes with large differences to the reference RTM scenario are only a fraction of the change in K_d for these scenes. The sensitivity analysis results underline the robust retrievability of K_d in the UV spectral range using DOAS VRS-fits in combination with a LUT-based approach, as it had been found for K_d-blue in Dinter *et al.* (2015) and Oelker *et al.* (2019).

Table 1: Maximum VRS fit (fit) and model errors provided in percent for the TROPOMI K_d-UVAB, K_d-UVA and K_d-blue retrievals <0.3 m^{-1}. Model errors are defined for not correctly parameterizing in the VRS cross section and LUTs RTM simulations the specific oceanic (CDOM absorption slope (CDOM-S) and coefficient (a_{CDOM}), the phytoplankton absorption (a_{ph}*)) and atmospheric parameters (aerosol optical thichness (AOD), wind speed (WS) and ozone concentration (O_3)). They are based on the sensitivity studies by Dinter *et al.* (2015) and presented in section 7.2.

K_d	fit	a_{CDOM}	CDOM-S	a_{ph}*	AOD	WS	O_3
UVAB	10	10	30	20	5	3	3
UVA	15	10	25	20	15	5	0
blue	20	20	25	10	20	10	0

K_d retrievals from OC sensors show low uncertainties for the visible spectral range. For the semi-analytical OC-CCI $K_d(490)$ algorithm, Lee *et al.* (2005c) report that for 90% of the retrieved $K_d(490)$ are within 25% of the in-situ measurement. It is not yet clear if similar quality can be reached for estimation of K_d-UV from the UV bands of current OC sensors or the UV wavelengths of the upcoming PACE mission. Due to lower intensity of the solar radiation in the UV, UV measurements are generally closer to the noise level. Also, atmospheric correction is more challenging at these short wavelengths (Frouin *et al.*, 2019). Indirect retrievals of K_d-UV from OC bands at visible wavelengths have also shown decent performance. For instance, Fichot *et al.* (2008) obtain $K_d(380)$ with mean relative error of about 10% and $K_d(340)$ and $K_d(325)$ with mean relative error around 18% from validation with 72 in-situ match-ups. They note that presence of MAA can cause larger errors on their retrieval at the shorter wavelengths. Because of the loose relationship between the spectral range below 360 nm and the visible, (Wang *et al.*, 2021) do not apply their neural network approach in this spectral range. We stress that a direct approach, analyzing the radiation backscattered in the UV wavelengths, should be further pursued to obtain K_d below 360 nm. In addition, the algorithm presented in this study provides an independent approach which can be used as verification for the K_d products from typical OC sensors which is especially important for the to date presented indirect K_d-UV OC data which are based on highly empirical approaches. Regions where empirical relationships might not hold are potentially identified.

Since the TROPOMI data acquisition started in May 2018, in-situ radiance measurements of underwater profiles have been very limited. The current in-situ matchup data set is too small to be included in a comprehensive error budget evaluation for our TROPOMI K_d retrievals. We use the maximum retrieval errors based on the relative VRS fit error (section 7.1) and the results from the retrieval sensitivity studies (provided in section 7.2 and Dinter *et al.* (2015)) as quantitative assessment of the TROPOMI K_d uncertainty (see Table 1). More precise calculations of the total error of the K_d retrieval are currently not possible since we do not know the distribution function of the optical and atmospheric constituents in the atmosphere and ocean. In addition, the uncertainty which is introduced for the K_d retrieval by the VRS offset correction is not quantified (see discussion in section 4.4.4). We expect that the TROPOMI K_d-blue error (at least for K_d <0.3 m^{-1}) will not be larger than those provided for OC-CCI. This is based on the rather low theoretical retrieval uncertainties, the low relative VRS fit factor errors and that for TROPOMI K_d-blue we obtained an agreement to the OC-CCI and OLCI K_d products within OC-CCI RMSD. Since K_d-UV retrievals even showed lower relative fit error and theoretical error for atmospheric parametrizations in SCIATRAN, we consider their total error to be similar or even lower.

7.4 Comparison to multispectral ocean color products

S5p ocean color product quality is estimated using triple collocation method as in Losa *et al.* (2017). Following data sets are used for the different products:

- S5p K_d blue, OLCI K_d 490 (empirical, Morel *et al.*, 2007b), OC-CCI K_d 490 (IOP-based, Lee *et al.*, 2005a)

More details on the multispectral products can be found in the S5POC VR.

7.4.1 Triple collocation

The triple collocation (TC) method (Stoffelen, 1998; Losa *et al.*, 2017) allows to estimate the absolute error variances ($\sigma^2_{\varepsilon_i}$), also called root mean squared difference (RMSD), of three collocated data sets with unknown uncertainties and with uncorrelated errors. The $\sigma^2_{\varepsilon_i}$ can be estimated from the unique terms covariance matrix (McColl *et al.*, 2014) (Q_{11}, Q_{12}, Q_{13}, Q_{22}, Q_{23},Q_{33}):

$$\sigma^2_{\varepsilon_i} = \begin{bmatrix} \sqrt{Q_{11} - \frac{Q_{12}Q_{13}}{Q_{23}}} \\ \sqrt{Q_{22} - \frac{Q_{12}Q_{23}}{Q_{13}}} \\ \sqrt{Q_{33} - \frac{Q_{13}Q_{23}}{Q_{12}}} \end{bmatrix} \tag{5}$$

Following Gruber *et al.* (2015) the fractional mean-squared-error (fMSE) can be calculated within the frame of the TC analysis:

$$fMSE_i = \frac{\sigma^2_{\varepsilon_i}}{\sigma^2_i} = \frac{1}{\beta^2_i \sigma^2_\Theta + \sigma^2_{\varepsilon_i}} = \frac{1}{1 + SNR_i}, \tag{6}$$

where β_i is a systematic bias of a particular data product with respect to the true state Θ; σ^2_i and $\sigma^2_{\varepsilon_i}$ denote the product variance and the product error variance, respectively. SNR_i is a signal-to-noise ratio. This fMSE criterion allows one to evaluate the plausibility of the TC based K_d uncertainty estimates. All details on the K_d triple collocation results can be found in the S5POC-VR (sections 6.1.5 to 6.1.8).

7.5 in-situ data

see section 8.

8 Validation

Table 2 summarizes information on *in situ* observations collected during cruises (PS113, PS121, MSM93) and surveys (FOCUS) in the test areas (Figure 2 in S5POC-RB, Figure A1 in S5POC-DP-AUM2) and used for S5POC product validation for the years 2018 to 2020. All details on the in validation results can be found in section 6.1.5 to 6.1.8 of the S5POC-VR (Bracher *et al.*, 2024).

Table 2: *In situ* observations used for S5POC evaluation.

Observation name	observation description	cruises/survey	test area
K_d	Light attenuation	PS113, PS121, MSM93	C, D

8.1 Match-up analyses

Collocations between *In situ* and S5p K_d products were defined differently for the products. Match-ups between geolocation of *in situ* and TROPOMI ground pixels for S5p K_d data were calculated using a loose criterion (within two days of the TROPOMI pixel) given the low number of regional available K_d *in situ* station data (in total 36 station data regional well distributed) complemented by about 450 Triaxus data. For each *in situ* measurement, TROPOMI match-ups were searched within 2 days and a radius of 5.5 km resulting in 45 (only 43 for UVAB) quality controlled matchups. For details see section 6.2.2 of the Bracher *et al.* (2024).

The match-up statistics are quantified by the metrics described in the OC-CCI Product User Guide (issue 2.0.5). The metrics includes RMSD, un-biased RMSD, bias, slope, intercept (type II regression) and Pearson coefficient of determination. In addition, the mean absolute error (MAE) is quantified. The metrics are computed as:

$$\text{RMSD} = \sqrt{\frac{1}{N}\sum_{i=1}^{N}(y_i - x_i)^2} \tag{7}$$

$$\text{Un-biased RMSD} = \sqrt{\frac{1}{N}\sum_{i=1}^{N}(Y_i - X_i)^2} \tag{8}$$

$$\text{Bias} = \frac{1}{N}\sum_{i=1}^{N}(y_i - x_i) \tag{9}$$

$$\text{MAE} = \frac{1}{N}\sum_{i=1}^{N}|y_i - x_i| \tag{10}$$

where x is the *in situ* observation, y the satellite data, and N the total number of samples. X corresponds to $x - mean(x)$ and analogous definition applies to Y. For PFT-CHL for the calculation of slope, intercept (type II regression) and Pearson coefficient of determination the PFT-CHL from *in situ* and TROPOMI are compared on Log10 scale. More details on the *in situ* matchup results can be found in sections 6.1.2 and 6.2.2 of S5POC-VR (Bracher *et al.*, 2024)).

References

Austin, R. W., & Petzold, T. J. 1981. *The Determination of the Diffuse Attenuation Coefficient of Sea Water Using the Coastal Zone Color Scanner*. Boston, MA: Springer US. Pages 239–256.

Blum, M, Rozanov, V V, Burrows, J P, & Bracher, A. 2012. Coupled ocean-atmosphere radiative transfer model in the framework of software package SCIATRAN: Selected comparisons to model and satellite data. *Advances in Space Research*, **49**(12), 1728–1742.

Bracher, A., & Bellido Rosas, A. J. 2024. *Exploitation of Sentinel-5-p (S5p) for Ocean Colour Products (S5POC) - S5p diffuse attenuation (Kd) product in Sentinel-5-p (S5p) Productive Algorithm Laboratory (PAL): Product User Manual (S5POC-PAL-PUM)*. Tech. rept. Alfred-Wegener Institut Helmholtz Zentrum fuer Polar- und Meeresforschung, and IUP, University Bremen.

Bracher, A, Vountas, M, Dinter, T, Burrows, J P, Röttgers, R, & Peeken, I. 2009. Quantitative observation of cyanobacteria and diatoms from space using PhytoDOAS on SCIAMACHY data. *Biogeosciences*, **6**(5), 751–764.

Bracher, A., Alvarado, L., Richter, A., Brotas, V., Brito, A., & Costa, M. 2022. *Sentinel-5P Ocean Colour: Impact Assessment. S5POC-IAR-D09 Version 1.1. 13 May 2022.* Tech. rept. Alfred Wegener Institute Helmholtz Centre for Polar and Marine Research; Institute of Environmental Physics, University of Bremen; Faculdade de Ciencias, Universidade de Lisboa; University of Victoria.

Bracher, A., Losa, S., & Oelker, J. 2024. *Exploitation of Sentinel-5-p (S5p) for Ocean Colour (S5POC): S5p diffuse attenuation (Kd) product in Sentinel-5-p (S5p) Productive Algorithm Laboratory (PAL), Validation Report, Version 1.0, 20 Dec 2024.* Tech. rept. Alfred Wegener Institute (AWI), Helmholtz Centre for Polar and Marine Research; Institute of Environmental Physics, University of Bremen.

Bracher, Astrid U., & Wiencke, Christian. 2000. Simulation of the effects of naturally enhanced UV radiation on photosynthesis of Antarctic phytoplankton. *Marine Ecology Progress Series*, **196**, 127–141.

Burrows, J. P., Platt, U., & Borrell, P. 2011. *Tropospheric Remote Sensing from Space*. Springer. Pages 1–65.

Chance, K, & Kurucz, R L. 2010. An improved high-resolution solar reference spectrum for earth's atmosphere measurements in the ultraviolet, visible, and near infrared. *Journal of Quantitative Spectroscopy and Radiative Transfer*, **111**(9), 1289–1295.

Dinter, T, Rozanov, V V, Burrows, J P, & Bracher, A. 2015. Retrieving the availability of light in the ocean utilising spectral signatures of vibrational Raman scattering in hyper-spectral satellite measurements. *Ocean Science*, **11**(3), 373–389.

Fichot, Cédric G., Sathyendranath, Shubha, & Miller, William L. 2008. SeaUV and SeaUVC: Algorithms for the retrieval of UV/Visible diffuse attenuation coefficients from ocean color. *Remote Sensing of Environment*, **112**(4), 1584 – 1602. Remote Sensing Data Assimilation Special Issue.

Fleischmann, Oliver, Hartmann, Matthias, Burrows, John, & Orphal, Johannes. 2004. New ultraviolet absorption cross-sections of BrO at atmospheric temperatures measured by time-windowing Fourier transform spectroscopy. *Journal of Photochemistry and Photobiology A: Chemistry*, **168**(11), 117–132.

Frouin, Robert J., Franz, Bryan A., Ibrahim, Amir, Knobelspiesse, Kirk, Ahmad, Ziauddin, Cairns, Brian, Chowdhary, Jacek, Dierssen, Heidi M., Tan, Jing, Dubovik, Oleg, Huang, Xin, Davis, Anthony B., Kalashnikova, Olga, Thompson, David R., Remer, Lorraine A., Boss, Emmanuel, Coddington, Odele, Deschamps, Pierre-Yves, Gao, Bo-Cai, Gross, Lydwine, Hasekamp, Otto, Omar, Ali, Pelletier, Bruno, Ramon, Didier, Steinmetz, François, & Zhai, Peng-Wang. 2019. Atmospheric Correction of Satellite Ocean-Color Imagery During the PACE Era. *Frontiers in Earth Science*, **7**, 145.

Gordon, Howard R, & McCluney, W R. 1975. Estimation of the Depth of Sunlight Penetration in the Sea for Remote Sensing. *Appl. Opt.*, **14**(2), 413–416.

Grainger, J F, & Ring, J. 1962. Anomalous Fraunhofer Line Profiles. *Nature*, **193**(feb), 762.

Gruber, A., Su, C.-H., Zwieback, S., Crow, W., Dorigo, W., & Wagner, W. 2015. Recent advances in (soil moisture) triple collocation analysis. *International Journal of Applied Earth Observation and Geoinformation*.

Haltrin, Vladimir I, & Kattawar, George W. 1993. Self-consistent solutions to the equation of transfer with elastic and inelastic scattering in oceanic optics: I. Model. *Appl. Opt.*, **32**(27), 5356–5367.

Joiner, J, & Vasilkov, A P. 2006. First results from the OMI rotational Raman scattering cloud pressure algorithm. *IEEE Transactions on Geoscience and Remote Sensing*, **44**(5), 1272–1282.

Lee, Zhong-Ping, Du, Ke-Ping, & Arnone, Robert. 2005a. A model for the diffuse attenuation coefficient of downwelling irradiance. *Journal of Geophysical Research: Oceans*, **110**(C2), C02016.

Lee, Zhong-Ping, Darecki, Miroslaw, Carder, Kendall L, Davis, Curtiss O, Stramski, Dariusz, & Rhea, W Joseph. 2005b. Diffuse attenuation coefficient of downwelling irradiance: An evaluation of remote sensing methods. *Journal of Geophysical Research: Oceans*, **110**(C2), C02017.

Lee, Zhong-Ping, Darecki, Miroslaw, Carder, Kendall L, Davis, Curtiss O, Stramski, Dariusz, & Rhea, W Joseph. 2005c. Diffuse attenuation coefficient of downwelling irradiance: An evaluation of remote sensing methods. *Journal of Geophysical Research: Oceans*, **110**(C2), C02017.

Losa, Svetlana N, Soppa, Mariana A, Dinter, Tilman, Wolanin, Aleksandra, Brewin, Robert J W, Bricaud, Annick, Oelker, Julia, Peeken, Ilka, Gentili, Bernard, Rozanov, Vladimir, & Bracher, Astrid. 2017. Synergistic Exploitation of Hyper- and Multi-Spectral Precursor Sentinel Measurements to Determine Phytoplankton Functional Types (SynSenPFT). *Frontiers in Marine Science*, **4**, 203.

Ludewig, Antje, Kleipool, Quintus, Bartstra, Rolf, Landzaat, Robin, Leloux, Jonatan, Loots, Erwin, Meijering, Peter, van der Plas, Emiel, Rozemeijer, Nico, Vonk, Frank, & Veefkind, Pepijn. 2020. In-flight calibration results of the TROPOMI payload on board the Sentinel-5 Precursor satellite. *Atmospheric Measurement Techniques*, **13**(7), 3561–3580.

Mason, John D, Cone, Michael T, & Fry, Edward S. 2016. Ultraviolet (250–550 nm) absorption spectrum of pure water. *Appl. Opt.*, **55**(25), 7163–7172.

McColl, Kaighin A, Vogelzang, Jur, Konings, Alexandra G, Entekhabi, Dara, Piles, María, & Stoffelen, Ad. 2014. Extended triple collocation: Estimating errors and correlation coefficients with respect to an unknown target. *Geophysical Research Letters*, **41**(17), 6229–6236.

Mobley, C.D., & Sundman, L.K. 2013. *HydroLight 5.2 - EcoLight 5.2 Technical Documentation*. Tech. rept. Sequoia Scientific, Inc.

Morel, A., Claustre, H., Antoine, D., & Gentili, B. 2007a. Natural variability of bio-optical properties in Case 1 waters: attenuation and reflectance within the visible and near-UV spectral domains, as observed in South Pacific and Mediterranean waters. *Biogeosciences*, **4**(5), 913–925.

Morel, André. 1988. Optical modeling of the upper ocean in relation to its biogenous matter content (case I waters). *Journal of Geophysical Research: Oceans*, **93**(C9), 10749–10768.

Morel, André, & Maritorena, Stéphane. 2001. Bio-optical properties of oceanic waters: A reappraisal. *Journal of Geophysical Research: Oceans*, **106**(C4), 7163–7180.

Morel, André, Huot, Yannick, Gentili, Bernard, Werdell, P. Jeremy, Hooker, Stanford B., & Franz, Bryan A. 2007b. Examining the consistency of products derived from various ocean color sensors in open ocean (Case 1) waters in the perspective of a multi-sensor approach. *Remote Sensing of Environment*, **111**(1), 69 – 88.

Oelker, J. 2021. *PhD Thesis*. Bremen: Department of Physics and Engineering, University Bremen, Bremen, Germany. Pages 1–150.

Oelker, Julia, Richter, Andreas, Dinter, Tilman, Rozanov, Vladimir V., Burrows, John P., & Bracher, Astrid. 2019. Global diffuse attenuation derived from vibrational Raman scattering detected in hyperspectral backscattered satellite spectra. *Opt. Express*, **27**(12), A829–A855.

Oelker, Julia, Losa, Svetlana N., Richter, Andreas, & Bracher, Astrid. 2022. TROPOMI-Retrieved Underwater Light Attenuation in Three Spectral Regions in the Ultraviolet and Blue. *Frontiers in Marine Science*, **9**, 787992.

O'Reilly, John E., Maritorena, Stéphane, Mitchell, B. Greg, Siegel, David A., Carder, Kendall L., Garver, Sara A., Kahru, Mati, & McClain, Charles. 1998. Ocean color chlorophyll algorithms for SeaWiFS. *Journal of Geophysical Research: Oceans*, **103**(C11), 24937–24953.

Perner, D, & Platt, U. 1979. Detection of nitrous acid in the atmosphere by differential optical absorption. *Geophysical Research Letters*, **6**(12), 917–920.

Pope, Robin M., & Fry, Edward S. 1997. Absorption spectrum (380–700 nm) of pure water. II. Integrating cavity measurements. *Appl. Opt.*, **36**(33), 8710–8723.

Remer, Lorraine A, Kleidman, Richard G, Levy, Robert C, Kaufman, Yoram J, Tanré, Didier, Mattoo, Shana, Martins, J Vanderlei, Ichoku, Charles, Koren, Ilan, Yu, Hongbin, & Holben, Brent N. 2008. Global aerosol climatology from the MODIS satellite sensors. *Journal of Geophysical Research: Atmospheres*, **113**(D14), D14S07.

Rothman, L S, Gordon, I E, Babikov, Y, Barbe, A, Benner, D Chris, Bernath, P F, Birk, M, Bizzocchi, L, Boudon, V, Brown, L R, Campargue, A, Chance, K, Cohen, E A, Coudert, L H, Devi, V M, Drouin, B J, Fayt, A, Flaud, J.-M., Gamache, R R, Harrison, J J, Hartmann, J.-M., Hill, C, Hodges, J T, Jacquemart, D, Jolly, A, Lamouroux, J, Roy, R J Le, Li, G, Long, D A, Lyulin, O M, Mackie, C J, Massie, S T, Mikhailenko, S, Müller, H S P, Naumenko, O V, Nikitin, A V, Orphal, J, Perevalov, V, Perrin, A, Polovtseva, E R, Richard, C, Smith, M A H, Starikova, E, Sung, K, Tashkun, S, Tennyson, J, Toon, G C, Tyuterev, Vl.G., & Wagner, G. 2013. The HITRAN2012 molecular spectroscopic database. *Journal of Quantitative Spectroscopy and Radiative Transfer*, **130**, 4–50.

Rozanov, V V, Rozanov, A V, Kokhanovsky, A A, & Burrows, J P. 2014. Radiative transfer through terrestrial atmosphere and ocean: Software package SCIATRAN. *Journal of Quantitative Spectroscopy and Radiative Transfer*, **133**, 13–71.

Rozanov, V V, Dinter, T, Rozanov, A V, Wolanin, A, Bracher, A, & Burrows, J P. 2017. Radiative transfer modeling through terrestrial atmosphere and ocean accounting for inelastic processes: Software package SCIATRAN. *Journal of Quantitative Spectroscopy and Radiative Transfer*, **194**, 65–85.

Sadeghi, A, Dinter, T, Vountas, M, Taylor, B B, Altenburg-Soppa, M, Peeken, I, & Bracher, A. 2012. Improvement to the PhytoDOAS method for identification of coccolithophores using hyper-spectral satellite data. *Ocean Science*, **8**(6), 1055–1070.

Serdyuchenko, A, Gorshelev, V, Weber, M, Chehade, W, & Burrows, J P. 2014. High spectral resolution ozone absorption cross-sections – Part 2: Temperature dependence. *Atmospheric Measurement Techniques*, **7**(2), 625–636.

Stoffelen, Ad. 1998. Toward the true near-surface wind speed: Error modeling and calibration using triple collocation. *Journal of Geophysical Research: Oceans (1978–2012)*, **103**(C4), 7755–7766.

Thalman, Ryan, & Volkamer, Rainer. 2013. Temperature dependent absorption cross-sections of O2–O2 collision pairs between 340 and 630 nm and at atmospherically relevant pressure. *Phys. Chem. Chem. Phys.*, **15**(37), 15371–15381.

van der Does, M., Korte, L. F., Munday, C. I., Brummer, G.-J. A., & Stuut, J.-B. W. 2016a. Particle size traces modern Saharan dust transport and deposition across the equatorial North Atlantic. *Atmospheric Chemistry and Physics*, **16**(21), 13697–13710.

van der Does, M., Korte, L. F., Munday, C. I., Brummer, G.-J. A., & Stuut, J.-B. W. 2016b. Particle size traces modern Saharan dust transport and deposition across the equatorial North Atlantic. *Atmospheric Chemistry and Physics*, **16**(21), 13697–13710.

van Geffen, J, Eskes, H, K., Boersma, J., Maasakkers, & Veefkind, J. 2019. *TROPOMI ATBD of the total and tropospheric NO2 data products Technical Report*. Tech. rept. Royal Netherlands Meteorological Institute.

Vandaele, A.C., Hermans, C., Simon, P.C., Carleer, M., Colin, R., Fally, S., Mérienne, M.F., Jenouvrier, A., & Coquart, B. 1998. Measurements of the NO2 absorption cross-section from 42 000 cm–1 to 10 000 cm–1 (238–1000 nm) at 220 K and 294 K. *Journal of Quantitative Spectroscopy and Radiative Transfer*, **59**(3), 171 – 184. Atmospheric Spectroscopy Applications 96.

Vasilkov, Alexander P, Joiner, Joanna, Gleason, James, & Bhartia, Pawan K. 2002a. Ocean Raman scattering in satellite backscatter UV measurements. *Geophysical Research Letters*, **29**(17), 14–18.

Vasilkov, Alexander P, Joiner, Joanna, Gleason, James, & Bhartia, Pawan K. 2002b. Ocean Raman scattering in satellite backscatter UV measurements. *Geophysical Research Letters*, **29**(17), 14–18.

Veefkind, J.P., Aben, I., McMullan, K., Förster, H., de Vries, J., Otter, G., Claas, J., Eskes, H.J., de Haan, J.F., Kleipool, Q., van Weele, M., Hasekamp, O., Hoogeveen, R., Landgraf, J., Snel, R., Tol, P., Ingmann, P., Voors, R., Kruizinga, B., Vink, R., Visser, H., & Levelt, P.F. 2012. TROPOMI on the ESA Sentinel-5 Precursor: A GMES mission for global observations of the atmospheric composition for climate, air quality and ozone layer applications. *Remote Sensing of Environment*, **120**, 70 – 83. The Sentinel Missions - New Opportunities for Science.

Vernet, Maria, Brody, Eric A., Holm-Hansen, Osmund, & Mitchell, B. Greg. 1994. *The Response of Antarctic Phytoplankton to Ultraviolet Radiation: Absorption, Photosynthesis, and Taxonomic Composition*. American Geophysical Union (AGU). Pages 143–158.

Vodacek, A., Blough, N., DeGrandpre, M., & Nelson, R. 1997. Seasonal variation of CDOM and DOC in the Middle Atlantic Bight: Terrestrial inputs and photooxidation. *Limnology and Oceanography*, **42**, 674–686.

Vountas, M, Rozanov, VV, & Burrows, JP. 1998. Ring effect: Impact of rotational Raman scattering on radiative transfer in Earth's atmosphere. *Journal of Quantitative Spectroscopy and Radiative Transfer*, **60**(6), 943–961.

Vountas, M, Richter, A, Wittrock, F, & Burrows, J P. 2003. Inelastic scattering in ocean water and its impact on trace gas retrievals from satellite data. *Atmospheric Chemistry and Physics*, **3**(5), 1365–1375.

Vountas, M, Dinter, T, Bracher, A, Burrows, J P, & Sierk, B. 2007. Spectral studies of ocean water with space-borne sensor SCIAMACHY using Differential Optical Absorption Spectroscopy (DOAS). *Ocean Science*, **3**(3), 429–440.

Walrafen, G E. 1967. Raman Spectral Studies of the Effects of Temperature on Water Structure. *The Journal of Chemical Physics*, **47**(1), 114–126.

Wang, Yongchao, Lee, Z., Wei, Jianwei, Shang, S., Wang, M., & Lai, Wendian. 2021. Extending satellite ocean color remote sensing to the near-blue ultraviolet bands. *Remote Sensing of Environment*, **253**, 112228.

Wolanin, A, Rozanov, V V, Dinter, T, Noël, S, Vountas, M, Burrows, J P, & Bracher, A. 2015a. Global retrieval of marine and terrestrial chlorophyll fluorescence at its red peak using hyperspectral top of atmosphere radiance measurements: Feasibility study and first results. *Remote Sensing of Environment*, **166**, 243–261.

Wolanin, A., Dinter, T., Soppa, M., & Bracher, A. 2015b. *Report on using radiative transfer modeling to develop a correction scheme and investigate the sensitivity of the improved PhytoDOAS (version3.0) algorithm. SY-4Sci Synergy R & D Study 4: Phytoplankton Functional Types (SynSenPFT)*. Tech. rept. Alfred Wegener Institute (AWI), Helmholtz Centre for Polar and Marine Research; Institute of Environmental Physics, University of Bremen.

*** END OF DOCUMENT ***